Time-Dependent Quantum Fluid Dynamics of the Photoionization of the He Atom Under an Intense Laser Field

BIJOY KR. DEY AND B. M. DEB*

Theoretical Chemistry Group, Department of Chemistry, Panjab University, Chandigarh 160014, India

ABSTRACT

A time-dependent (TD), nonperturbative quantum fluid density functional equation of motion, developed in our laboratory, is numerically solved for studying the photoionization dynamics of the He atom under an intense, ultrasharp, ultrashort laser pulse. The generalized nonlinear Schrödinger equation is obtained through a hydrodynamical continuity equation and an Euler-type equation of motion. It yields the electron density, effective potential surface, and other density-based quantities from start to finish. Starting from the ground-state Hartree–Fock density for He at $t = 0$, various singlet and triplet states of singly and doubly excited (autoionizing) He as well as several states of He^+ have been identified in the time-evolved electron density, by a Fourier transformation of the time variable of the complex autocorrelation function. Computer visualizations of the TD difference density and difference potential show distinctly nonlinear and extremely interesting geometrical features of the oscillating atom. Detailed mechanistic routes for multiphoton, sequential, and above-threshold ionization have been obtained, each route involving many states. The present, comprehensive method reveals the important physical features of the atom–laser interaction and the calculated results are consistent with current experimental and theoretical results. This emphasizes the validity of the hydrodynamical approach for studying TD quantum mechanical phenomena. © 1995 John Wiley & Sons, Inc.

*To whom correspondence should be addressed. Also from the Jawaharlal Nehru Centre for Advanced Scientific Research, Indian Institute of Science Campus, Bangalore-560012, India.

Introduction

When atoms are subjected to intense (10^{13} W cm^{-2} or more), ultrashort (femtosecond regime) laser pulses, they are not only bombarded by many more photons than are available in the usual photophysical processes, their electrons are also subjected to optical electric fields comparable to or even exceeding the nuclear field strengths. As a result, extremely interesting phenomena, some of some of which may be counterintuitive, are observed [1–28]. While the subject of atom–laser interaction is relatively old, interest in the subject has blossomed in the last decade, due mainly to the availability of intense and ultrafast lasers of varying frequencies and pulse durations as well as sophisticated quantum mechanical methodologies.

Under the laser field, the atom primarily responds by photoionization and photoemission, both of which are interrelated phenomena. Depending on the frequency and field strength of the laser as well as the ionization potential of the atom, photoionization can involve a tunneling mechanism [18, 22, 23, 29] or a multiphoton mechanism [19, 20, 22, 29]. Under the latter, above-threshold ionization (ATI) with well-defined peaks in the photoelectron spectrum occurs. The ATI is due to mutiphoton excitation to the continuum [19, 20, 22]. Besides ATI, sequential ionization [21], in which atom A loses its electrons in different states of ionization, A^{n+}, as well as over-the-barrier ionization [1] also occurs. In superintense laser fields of 10^{17} W cm^{-2} or more, ionization suppression or stability can result [1, 25, 30]; this appears to be contrary to intuition.

ATI is associated with the generation of high-order harmonic frequencies (odd multiples of the laser frequency with a linearly polarized laser field) [1, 11, 14, 15, 19, 20, 28]; a multiple of up to 133 or more can be observed. The harmonic spectra are characterized by a rapid decrease in intensity for low-order harmonics, followed by a plateau where the harmonic intensity decreases relatively slowly, and then there is an abrupt cutoff beyond which no harmonics are observed. The striking difference between electron emission and photoemission is that while the harmonic spectrum has a cutoff the ATI spectrum does not.

In view of the high laser intensity, perturbative quantum mechanical (QM) treatments cannot be resorted to for explaining the above phenomena. Burnett et al. [1] summarized the theoretical, non-perturbative methodologies employed so far to deal with these multiphoton processes. These are the essential-states methods (see, e.g., [31]); Volkov final-state theories (see, e.g., [32]); Floquet theory (see, e.g., [16]); numerical integration of the time-dependent (TD) Schrödinger equation for one-dimensional systems; and TD Hartree–Fock (HF) calculations for many-electron systems [1, 5–15]. Monte Carlo calculations (see, e.g., [33]) as well as relatively simpler and semiclassical models/theories have also been presented [17, 20, 23, 24, 26–28]. However, TDQM calculations on realistic systems are still extremely difficult and time-consuming to perform.

The object of this article is to propose a nonperturbative, comprehensive TDQM method for realistic computations in more than one spatial dimension for actual atoms. The work is prompted by the following considerations: (1) One requires a holistic and computationally tractable TDQM method which can deal with various facets of the atom–laser interaction so that subtle interconnections between the different facets can be understood. (2) The detailed mechanisms, from start to finish, of the various dynamical processes can be understood in a much more transparent and physical manner by studying the TD changes in various density-based quantities and the potential surface. (3) Since ionization eventually leads to plasma formation, the proposed methodology might employ the hydrodynamical analogy to quantum mechanics (see [34, 35] for review). (4) Because the interacting atom is a strongly driven nonlinear system, one should employ a nonlinear equation (e.g., a density-based equation) for the space–time evolution of the system. It is quite likely that, depending on the parameters of the interaction, the system might reveal quantum chaos [36], solitons, and bifurcations; thus any striking change in the nature of the process may be due to bifurcation while the phenomenon of stability under superintense fields might indicate solitary wave or soliton formation. (5) For an N-electron system, one might solve only one equation, and not N coupled equations, so that computational effort does not increase significantly with the number of electrons. We feel that these objectives might be attained by the present approach, which is an amalgamation of

density functional theory (DFT) [37, 38] and quantum fluid dynamics (QFD) [34, 35, 39–41].

In the following section, we describe the hydrodynamical equation for a helium atom under an intense laser field. The third section discusses the method of calculation, while the fourth section interprets the results (numbers and computer visualizations). Finally, the fifth section concludes that the main physical features of the atom–laser interaction are reproduced by the present method.

The Time-dependent Quantum Fluid Dynamical Equation

The relation between QFD and DFT has been intimate and well established [42–44]. In fact, this relation had provided the foundation for the development of TDDFT (see [45] for a review). Deb et al. [39, 40, 42] showed that the TD quantum mechanical electron density $\rho(\mathbf{r}, t)$ in a many-electron system behaves as a continuous, "classical" fluid, governed by two equations, viz., a continuity equation and a Navier–Stokes-type equation of motion (EOM) in three-dimensional space, as follows (atomic units employed throughout this article, unless otherwise specified):

$$\frac{\partial \rho(\mathbf{r}, t)}{\partial t} + \nabla \cdot (\rho \mathbf{U}) = 0, \tag{1}$$

$$\frac{\partial S(\mathbf{r}, t)}{\partial t} + \frac{1}{2}(\nabla S)^2 + \frac{\delta G[\rho]}{\delta \rho}$$
$$+ \int \frac{\rho(\mathbf{r}', t)}{|\mathbf{r} - \mathbf{r}'|} d\mathbf{r}' + V_{ext}(\mathbf{r}, t) = 0, \tag{2}$$

where the universal functional $G[\rho]$ consists of kinetic and exchange-correlation (XC) contributions, $V_{ext}(\mathbf{r}, t)$ is the external potential governing the TD phenomenon, and the velocity vector $\mathbf{v}(\mathbf{r}, t) = \nabla S(\mathbf{r}, t)$.

Equations (1) and (2) can be combined into a *single* equation by defining the hydrodynamical function in polar form,

$$\Psi(\mathbf{r}, t) = \rho^{1/2}(\mathbf{r}, t) \exp[iS(\mathbf{r}, t)], \tag{3}$$

and eliminating the velocity potential $S(\mathbf{r}, t)$ between Eqs. (1) and (2). The result is a generalized nonlinear Schrödinger equation (GNLSE) which

takes the following form [46] in cylindrical coordinates ($0 \le \bar{\rho} \le \infty$, $-\infty \le \bar{z} \le +\infty$, $0 \le \bar{\phi} \le 2\Pi$):

$$\left[-\tfrac{1}{2}\nabla^2_{\bar{\rho}, \bar{z}} + V_{eff}(\rho; \bar{\rho}, \bar{z}, t) \right] \Psi(\bar{\rho}, \bar{z}, t)$$
$$= i \frac{\partial}{\partial t} \Psi(\bar{\rho}, \bar{z}, t), \tag{4}$$

where

$$V_{eff}(\rho; \bar{\rho}, \bar{z}, t) = V_x[\rho] + V_c[\rho]$$
$$+ U(\bar{\rho}, \bar{z}, t) + V_l(\bar{z}, t). \tag{5}$$

In Eq. (4), the azimuthal angle $\bar{\phi}$ has been integrated out. Within a local density approximation, we employ the Dirac expression for the exchange potential $V_x[\rho]$ and a Wigner-type parametrized expression for the correlation potential $V_c[\rho]$ because a combination of the two is a very good approximation to $V_{xc}[\rho]$ due to a partial cancellation of errors [47]. $U(\bar{\rho}, \bar{z}, t)$ is the electrostatic potential and $V_l(\bar{z}, t)$ is the interaction potential between the many-electron system and the external field, taking the latter along the $\bar{z}$-axis. Therefore, these individual terms of the right-hand side of Eq. (5) may be written as

$$V_x[\rho] = -(4/3)c_x \rho^{1/3}; \quad c_x = (3/4\Pi)(3\Pi^2)^{1/3} \tag{6}$$

$$V_c[\rho] = -\frac{9.810 + 28.583\rho^{-1/3}}{(9.810 + 21.437\rho^{-1/3})^2} \tag{7}$$

$$U(\bar{\rho}, \bar{z}, t) = -\frac{Z}{r}$$
$$+ \int \frac{\rho(\mathbf{r}', t)}{|\mathbf{r} - \mathbf{r}'|} \bar{\rho}' \, d\bar{\rho}' \, d\bar{z}' \, d\bar{\phi}' \tag{8}$$

$$r = (\bar{\rho}^2 + \bar{z}^2)^{1/2} \tag{9}$$

$$\rho(\mathbf{r}, t) = \rho(\bar{\rho}, \bar{z}, t) = |\Psi(\bar{\rho}, \bar{z}, t)|^2 \tag{10}$$

$$V_l(\bar{z}, t) = -E_0 f(t)\sin(\omega t)\bar{z}, \tag{11}$$

where Z is the nuclear charge of the atom and a linearly polarized laser field is taken for V_l. The laser intensity (I) is taken as 5.6×10^{13} W cm^{-2} (8.70036×10^{-3} au). Using the relation

$$I = \frac{1}{8\Pi} c E_0^2, \tag{12}$$

where c is the speed of light, we obtain $E_0 = 0.03995$ au. In Eq. (11), $f(t)$ is the temporal pulse-

shape function, represented by a Gaussian, as follows:

$$f(t) = \begin{cases} e^{-\alpha(t-t_0)^2}, & t < t_0 \\ 1, & t \geq t_0, \end{cases} \qquad (13)$$

where $\alpha = 2.59559 \times 10^{-4}$ au, $t_0 = 10\Pi/\omega_L = 227.32755$ au, and the laser frequency $\omega_L = 0.13819674$ au, corresponding to $\lambda = 329.7$ nm. Thus, the Gaussian function is centered at $\cong 5.5$ fs and has a width of $\cong 2.5$ fs. Each oscillation period of the laser field is 45.46551 au (1 au of time = 0.0241889 fs). This hypothetical laser was chosen for computational economy. However, the present calculated results reproduce the main features of the atom–laser interaction obtained experimentally with real lasers.

Equations (4)–(11) describe the complete dynamics of the atom–laser interaction process through the time-evolution of the hydrodynamical function $\Psi(\mathbf{r}, t)$ [Eq. (3)], which yields the TD charge density and current density, as well as the time-evolution of the pulsating effective potential $V_{eff}(\rho; \mathbf{r}, t)$ on which the process occurs. The significance of Eq. (4) has been discussed previously [39, 40]. It is clear that under the strong laser perturbation many excited and ionized states of the He atom will mix with the unperturbed, ground state (at $t = 0$). Therefore, a major assumption in this work is that the xc potential, given by Eqs. (6) and (7), is also valid for excited states. While we are forced to make this assumption due to the current inadequate knowledge about the universal xc energy functionals, it can nevertheless be said that, in view of the high accuracy of the present calculations and the high magnitude of the interaction involved, it is unlikely that the introduction of nonlocal and/or state-dependent corrections to the xc functionals would introduce any major change in the qualitative physical conclusions derived from our results. In any case, such corrections for excited states, as and when they become available, can readily be incorporated into Eq. (4). The kinetic-energy part is dealt with by the Laplacian in Eq. (4).

It is worthwhile to note that since the density viewpoint gives rise to nonlinear differential or integrodifferential or algebraic equations [47], it is a natural choice for dealing with a strongly driven, nonlinear system such as an atom under an intense laser field. The present density approach proceeds much beyond the linear-response approximation.

The highly nonlinear GNLSE [Eq. (4)] calculates $\rho(\bar{\rho}, \bar{z}, t)$ to all orders of change under the interaction. This $\rho(\bar{\rho}, \bar{z}, t)$ is then employed to calculate the TD expectation value of the oscillating dipole moment which is essentially the palm print of the interaction. Thus, within the current status of TDDFT [45], Eq. (4) provides a rigorous TDQM formalism based on single-particle densities as basic variables. A major advantage of Eq. (4) is that it is amenable to high-accuracy computation over a large number of time steps and computational labor or that its cost does not increase significantly with increase in the number of electrons. Depending on the nature of the interaction, Eq. (4) can also reveal the nonlinear features, if any, in the dynamics, such as solitons and chaos.

Method of Calculation

The following are the four main steps in the numerical solution of the GNLSE [Eq. (4)]:

1. Discretization of the cylindrical grid ($\bar{\rho}, \bar{z}$), after integrating out the azimuthal angle ϕ, as

$$\left. \begin{array}{ll} \bar{\rho} = x^2 \\ x = lh, & l = 1, \ldots, N_1 \\ \bar{z} = -\bar{z}_0 + mh, & m = 1, \ldots, N_2 \end{array} \right\}, \qquad (14)$$

$$\bar{z}_0 = 3.3, \quad h = 0.03, \quad N_1 = 75, \quad N_2 = 221$$

where $\bar{z}_0$ is half the length of the cylinder. This discretization effectively deals with the singularity problem arising out of the Z/r term in Eq. (8).

2. Discretization of the time domain selected for studying the dynamics of the process, as

$$t = n\,\Delta t, \qquad n = 1, \ldots, N_3$$

$$\Delta t = \begin{cases} \dfrac{\Pi}{2700\,\omega_L}, & \text{up to the 30th time step} \\ \dfrac{\Pi}{90\,\omega_L}, & \text{after the 30th time step} \end{cases} \qquad (15)$$

$$N_3 = 3000.$$

3. Calculation of the complex nonlinear time propagator, $e^{\Delta t \hat{L}}$, in the above-discretized $(\bar{\rho}, \bar{z})$ space, where [46]

$$\hat{L} = -\frac{1}{8x^2 i}\frac{\partial^2}{\partial x^2} - \frac{1}{8x^3 i}\frac{\partial}{\partial x}$$
$$-\frac{1}{2i}\frac{\partial}{\partial \bar{z}^2} + \frac{V_{eff}}{i}. \quad (16)$$

4. Operation with this time propagator on the hydrodynamical function $\Psi(\bar{\rho}, \bar{z}, t)$ for generating the corresponding function at an advanced time, $t + \Delta t$, viz.,

$$\Psi(\bar{\rho}, \bar{z}, t + \Delta t) = e^{\Delta t \hat{L}}\Psi(\bar{\rho}, \bar{z}, t). \quad (17)$$

Starting with the Hartree–Fock (HF) density [48] for the ground state of He at $t = 0$ and following the above steps 1–4, the numerical solution of Eq. (4) yields the hydrodynamical functions

$$\Psi(\bar{\rho}, \bar{z}, \Delta t), \Psi(\bar{\rho}, \bar{z}, 2\Delta t), \ldots, \Psi(\bar{\rho}, \bar{z}, N_3\Delta t).$$

From these solutions, all TD density-based properties at a particular instant can be calculated. The complete numerical scheme as well as the finite-difference and stability analysis [46] have been discussed elsewhere. All computations have been performed in double precision on an APOLLO-DN3000 workstation.

Under the multiphoton interaction, the time-evolved density becomes a complicated mixture of densities from a large number of excited and ionized states of the He atom, including the continuum. To unscramble this mixture, the following quantities are reported here:

(i) *Electronic charge*—The total electronic charge, $N(t)$, is given by

$$N(t) = \int \rho(\bar{\rho}, \bar{z}, t)\bar{\rho}\, d\bar{\rho}\, d\bar{z}\, d\tilde{\phi};$$
$$N(0) = 1.99939. \quad (18)$$

This indicates the progress of ionization with time. To find out how the electron density oozes out of the atom, one needs to look at the system through a window, defined by $-1.5 \le x \le 1.5$, $-2.55 \le \bar{z} \le 2.55$. The electronic charge within this win-

dow (w) is given by

$$N_w(t) = \int_w \rho(\bar{\rho}, \bar{z}, t)\bar{\rho}\, d\bar{\rho}\, d\bar{z}\, d\tilde{\phi};$$
$$N_w(0) = 1.965169. \quad (19)$$

(ii) TD *difference density*—This shows the *dynamical* nature of the reorganization of electron density due to the interaction and is calculated as

$$\Delta\rho(\bar{\rho}, \bar{z}, t) = \rho(\bar{\rho}, \bar{z}, t)$$
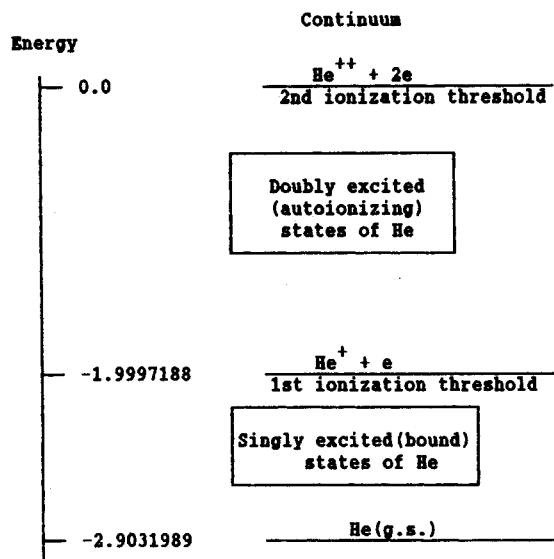$$- \rho(\bar{\rho}, \bar{z}, \Delta t_2), \quad (20)$$

where Δt_2 is the second time step, chosen instead of $t = 0$ because the ground-state HF density is not a solution of Eq. (4). The positive values of $\Delta\rho$ in a region denote a buildup of electronic charge in that region, whereas the negative values indicate a depletion of electronic charge.

(iii) TD *difference effective potential*—The valleys and peaks in V_{eff} oscillate in time. Such oscillations correspond to the buildup and depletion of electronic charge in the corresponding regions. The changes in the pulsating shape of V_{eff} are clearly seen from the difference effective potential,

$$\Delta V_{eff}(\bar{\rho}, \bar{z}, t) = V_{eff}(\bar{\rho}, \bar{z}, t)$$
$$- V_{eff}(\bar{\rho}, \bar{z}, \Delta t_2). \quad (21)$$

(iv) *Excitation and ionization probability, $p_{ei}(t)$* —To explain the *mechanisms* of multiphoton excitation and ionization of He, the ionization profile (Fig. 1) of the atom provides a starting point. One may envisage the following main routes for excitation and ionization, each route involving many excited/ionized states ($g.s.$, *, and ** denote ground state, singly excited, and doubly excited state, respectively):

Route a:	He ($g.s.$) → He*
Route b:	He ($g.s.$) → He**
Route c:	He($g.s.$)
	→ He (continuum)
Route d:	He**
	→ He$^+$($g.s$)/He^{+*} + e
Route e:	He (continuum)
	→ He^{2+} + $2e$.

Energy

Continuum

— 0.0

$\underline{He^{++} + 2e}$
2nd ionization threshold

┌─────────────────┐
│ Doubly excited │
│ (autoionizing) │
│ states of He   │
└─────────────────┘

— -1.9997188

$\underline{He^{+} + e}$
1st ionization threshold

┌─────────────────┐
│ Singly excited(bound) │
│ states of He   │
└─────────────────┘

— -2.9031989

$\underline{He(g.s.)}$

FIGURE 1. Ionization profile of the He atom (au); g.s. means ground state.

Other possible routes for excitation are

Route f: He* → He**
Route g: He* → He (continuum)
Route h: He** → He (continuum)
Route i: He⁺*

        → He⁺ (continuum),

and another route for ionization could be

Route j: He⁺ (continuum)

        → He²⁺ + e.

Route d indicates ionization via the doubly excited (autoionizing) states, while routes c and e indicate above-threshold ionization (ATI) in which two electrons are "simultaneously" expelled by the atom. The extent to which these various routes contribute to the multiphoton excitation and ionization processes varies with time.

The calculation of the cross section for each of the above individual routes has not been attempted in this study and is a problem for future investigation. Essentially, this requires one to determine the mixing coefficients of all the states, corresponding to a particular route, which appear in the time-evolved density. Writing the time-evolved hydrodynamical func-

tion $\Psi(\mathbf{r}, t)$ as

$$\Psi(\mathbf{r}, t) = c_0(t)\psi_0(\mathbf{r}) + \sum_i c_{ai}(t)\psi_{ai}(\mathbf{r})$$

$$+ \sum_j c_{bj}(t)\psi_{bj}(\mathbf{r})$$

$$+ \sum_k c_{ck}(t)\psi_{ck}(\mathbf{r})$$

$$+ \cdots + \text{cross terms}, \qquad (22)$$

where ψ_0 is the initial, ground-state function and $\psi_{ai}(\mathbf{r})$, $\psi_{bj}(\mathbf{r})$, etc., are functions corresponding to the various states belonging to routes a, b, etc., with the TD mixing coefficients $c_{ai}(t), c_{bj}(t)$ etc. The cross terms in Eq. (22) take care of the fact that $\Psi(\mathbf{r}, t)$ does not obey a linear superposition principle. Taking $\Psi(\mathbf{r}, t)$ as normalized to unity and assuming the cross terms to be small, the quantities $\sum |c_{ai}(t)|^2$, $\sum |c_{bj}(t)|^2$, etc., may be interpreted as the probabilities for routes a, b, etc. The probability for a route divided by the laser intensity gives a measure of the photoabsorption cross section for the route.

We define the total probability for all the above routes as the excitation and ionization probability $p_{ei}(t)$, where

$$p_{ei}(t) = 1 - p_{g.s.}(t). \qquad (23)$$

Here, $p_{g.s.}(t)$ is the TD ground-state probability of the He atom, given by

$$p_{g.s.}(t) = |\langle \Psi(0)|\Psi(t)\rangle|^2 \qquad (24)$$

and normalized to unity at $t = 0$.

(v) The expectation value of the TD (oscillating) *dipole moment* along the z-axis is given by [see also Eqs. (19) and (20)]

$$\mu^z(t) = \int \rho(\vec{\rho}, \vec{z}, t)\vec{z}\vec{\rho}\, d\vec{\rho}\, d\vec{z}\, d\vec{\phi}. \qquad (25)$$

This oscillating dipole moment will emit radiation, including overharmonic generation $n\omega_L$, where n is an odd integer. In the present calculations, $n = 3$–21 have been observed [46]. Thus, as has been remarked by a number of workers [20, 26], the processes of multiphoton excitation, ionization, and photoemission are intimately linked. The detailed mechanism, including the principal routes, each of which involves many transitions, for photoemis-

sion has been discussed elsewhere [46]. The dipole moment is an ensemble of a large number of state-to-state transition moment integrals, $\langle \psi_{ni}|\hat{z}|\psi_{mj}\rangle(t)$, where n and m correspond to two energy levels and i, j correspond to degenerate sets.

(vi) *The energy spectrum*—To identify the various states and their percent contributions to the time-evolved density, it is necessary to compute the *energy spectrum* [49] by a fast Fourier transformation (FFT) of the time variable in the complex autocorrelation function, $\langle \Psi(0)|\Psi(t)\rangle$. The autocorrelation function yields a measure of the correlation of the system at time t with its initial state or, equivalently, of the survival of the initial (ground) state due to the interaction. The FFT transforms the time grid defined as $t_n = n\,\Delta t$, $n = 0, 1, \ldots, N$, to its conjugate frequency grid, f, with grid points

$$f_j = \begin{cases} (j-1)/(N\Delta t), \\ \quad 1 \le j \le N/2 + 1 \\ -(N/2 + 1 - j)/(N\Delta t) \\ \quad 2 \le j \le N/2 - 1. \end{cases} \quad (26)$$

The Nyqvist critical frequency, $f_{N/2} = 1/(2\,\Delta t)$. The FFT requires that the total sampled values of N must be an integer power of 2. For the present calculations, $N = 2^{11} = 2048$ ($t = 517.29647$ au), although we have allowed the density to evolve up to 3000 time steps

$$[\,t = (2971/90)(\Pi/\omega_L)$$
$$= 750.4335 \text{ au} = 18.15216 \text{ fs}].$$

The energy spectral density, $\text{ESD}(\omega)$, is the probability per unit time per unit volume for a state of energy $\hbar\omega$. This is defined through the Fourier transform as

$$\text{ESD}(\omega) = \left| \int_0^\infty e^{-i\omega t}\langle \Psi(0)|\Psi(t)\rangle \, dt \right|^2,$$
$$-\infty \le \omega \le +\infty, \quad (27)$$

where "infinite" time is 517.29647 au (12.512833 fs), as mentioned above. The negative values of ω correspond to excited/ionized states of the He atom below the double-ionization threshold,

whereas the positive values of ω correspond to continuum states. The percent contribution of the jth state to the ESD is given by

$$\frac{\text{ESD}(\omega_j)}{\text{TSD}} \times 100, \quad (28)$$

where $\text{ESD}(\omega_j)$ is obtained by replacing ω in Eq. (27) with the specific value ω_j and TSD is the total spectral density calculated by using the triangle approximation as

$$\text{TSD} = \frac{1}{2} \sum_j \text{ESD}(\omega_j)\, d\omega_j, \quad (29)$$

where $d\omega_j$ is the width of the resonance at ω_j.

(vii) *The rate and cross section of photoionization*—The average photoionization rate (R) is defined as

$$R = \frac{1}{t_x - t_0} \int_{t_0}^{t_x} \frac{dN(t)}{dt}\, dt, \quad (30)$$

where $N(t)$ is given by Eq. (18), $t_0 = 0$, and $t_x = 750.4335$ au (18.15216 fs). The total photoionization cross section is given by

$$\sigma_{ion} = \frac{R}{I}, \quad (31)$$

where I is the laser intensity.

Result and Discussion

Figure 2 depicts the laser electric field $E(t)$ as a function of time, while Table I lists the values of the dipole moment $\mu^z(t)$ at selected intervals. Starting from a zero value, the laser field as well as the dipole moment begins to build up at $t \cong 130$ au. The nonlinear oscillations in $\mu^z(t)$ are much faster than are the oscillations of the laser field, indicating nonresonant absorption. Initially, the amplitude of $\mu^z(t)$ increases with time, indicating the onset of polarization and ionization. As ionization increases, this amplitude decreases. The oscillations in $\mu^z(t)$ indicate an apparently chaotic pattern. Indeed, quantum chaos has been observed in both the calculated power spectrum and rate spectrum for photoemission [36].
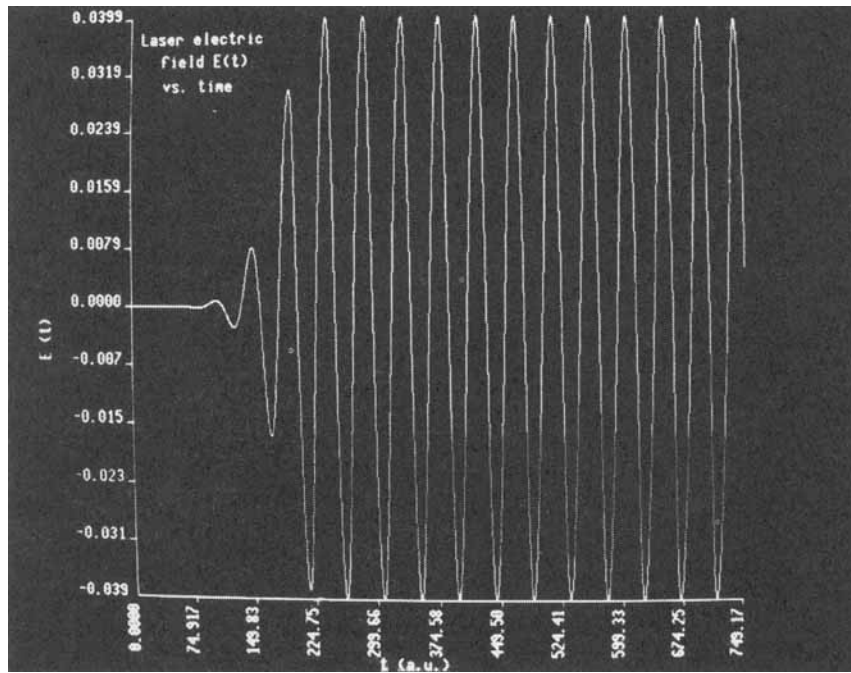
FIGURE 2. Laser electric field $E(t)$ plotted against t, in au. Due to the Gaussian pulse-shape function [Eq. (13)], $E(t)$ begins to build up at $t \cong 130$ au. About 12.5 oscillations are shown.

Figure 3 depicts the oscillating total electronic charge $N(t)$, given by Eq. (18), while Table I lists the oscillating values of $N_\omega(t)$ [Eq. (19)] at selected times. It is clear that the decay in $N(t)$ is not exponential and the onset of ionization is somewhat slow. Thus, at $t = 131.6$ au, when the field is building up, the atom has already lost only 0.7% of its electronic charge, while the window (see Fig. 4) has lost $\cong 36\%$ of its own electronic charge. At the last time step, these values are $\cong 18\%$ and 54.5% respectively. It is clear that there is an ongoing "tug-of-war" for the electron density between the nucleus and the laser field—which the nucleus gradually loses—such that the electron density is depleted from regions near the nucleus (e.g., the window) by the field and built up elsewhere, but a part of the density keeps returning to regions near the nucleus. Such large-amplitude nonlinear oscillations are characteristic of multiphoton ionization (MPI). As we will see later, electron density gradually oozes out of the atom along the field direction ($\hat{z}$).

Evaluation of the adiabaticity or Keldysh [29] parameter γ confirms that the present atom–laser interaction is in the MPI regime ($\gamma \geq 1$), where

$$\gamma = (U_I/2U_P)^{1/2}. \qquad (32)$$

In Eq. (32) U_I is the ionization potential (IP) of the atom and U_P is the ponderomotive potential (mean kinetic energy acquired by a free electron in the oscillating laser field of strength ε), given by

$$U_P = \frac{e^2\varepsilon^2}{4m_e\omega^2} \text{ eV} = 9.33 \times 10^{-14}I\lambda_L^2, \qquad (33)$$

where I is in W cm^{-2} and λ_L is in μm. $\gamma \leq 1$ corresponds to the regime of tunneling ionization. From Figure 1, taking $\varepsilon = E_0 = 0.03995$ au, we obtain $\gamma = 4.74$, 7.07, and 8.34 for the first, second and total ionization, respectively. It may also be noted that for these three ionizations I_{th}, the threshold intensity for a dc field ionization, is 0.0104, 0.2499, and 1.110 au, respectively, where [18] $I_{th} = U_I^4/(16Z^2)$; these values are larger than the present $I = 0.00870036$ au. The oscillating net multiphoton excitation and ionization probability, from Eq. (23), is depicted in Figure 4, while the oscillating ground-state probability values from Eq. (24) are given in Table I. We notice from Figures 3 and 4 that excitation is noticeably faster than is ionization and, therefore, the former precedes the latter. For example, at $t \cong 131.6$ au, the ground-state probability has decreased by 57%, whereas $N(t)$ has decreased by only 0.7%. This is in accord
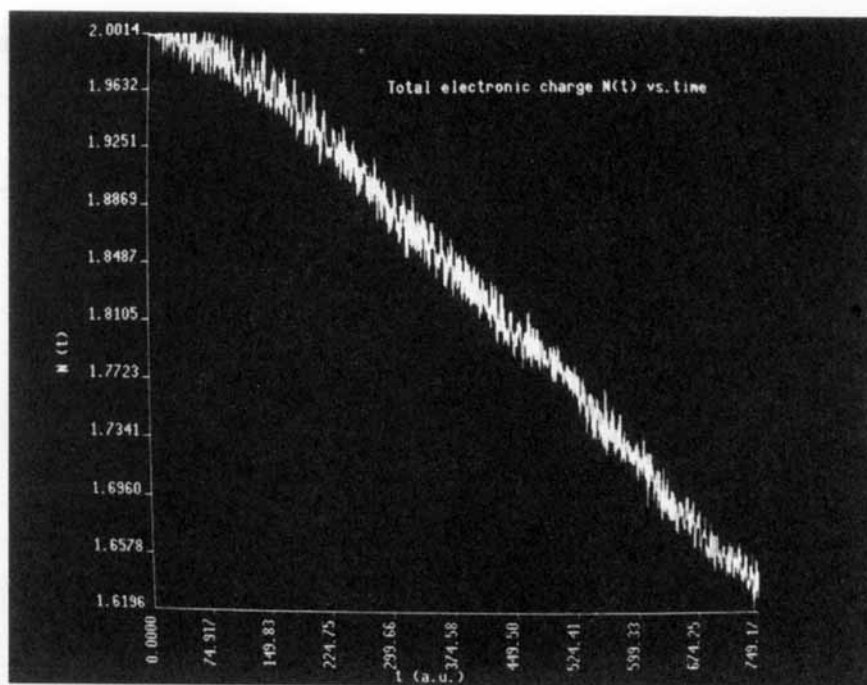
FIGURE 3. Rapidly oscillating total electronic charge $N(t)$ plotted against t, in au. $N(0) = 1.999399$; $N(750.4335) = 1.635948$.

with the observation that a high degree of excitation should occur by the pulse time, Π/R_f, where the two-level Rabi frequency $R_f = \mu E_0/\hbar$, μ being the transition dipole. Taking $\mu = 1.0$ au this pulse time is 78.638 au, i.e., 1.902 fs. At the last time step, $p_{g.s.}(t)$ has decreased by 74%, whereas ionization is only 18%. Thus, the contribution of ionized states of He to Figure 4 is much less than that of its various excited states. With a pulse of duration much longer than 18 fs, these two percentages should be comparable in magnitude.

The energy spectrum corresponding to $\rho(\mathbf{r}, t)$ at $t = 12.512833$ fs is shown in Figure 5, while a detailed analysis of the spectrum is given in Tables II–V where a large number of the peaks in Figure 5 has been identified in terms of He* states, He** states, He$^+$ states, and continuum states (not shown in Fig. 5). Table IV shows that in Figure 5 the peaks labeled a, b, c, j, and r correspond to He$^+$ states with $n = 13, 7, 5, 3$, and 2, respectively. Table III shows that all the other labeled peaks in Figure 5 correspond to He** states which are autoionizing (resonance). The identification of He* states, which occur with relatively low ESD and low percent contribution to the TSD compared to other states, is shown in Table II. Table V shows

the continuum states with the largest ESD. A large number of continuum states are involved, all of which are not shown in Table V. A practical limit is given by the continuum state of energy 12.32839 au, with ESD 0.128327 au and contribution to the TSD of 0.0014%. Under the present conditions, the high-harmonic cutoff for photoemission is given by [15]

$$n_{max} \cong (U_i + 3U_p)/\omega_L = 21, \tag{34}$$

whereas at $t = 12.512833$ fs, $n = 13$ was observed in these calculations with moderate power spectral density (PSD) and rate spectral density (RSD) [36] as one of the dominant harmonic generations. However, $n = 15–21$ was also observed [36] with low PSD and RSD. Thus, in our calculations, ATI continues well beyond the high-harmonic cutoff, in agreement with experimental [19, 20] and other theoretical [20] results.

The matching between the present calculated energy values and those of the various excited/ionized states of He is generally excellent. The discrepancy in our calculated energies is 0.02–3.9% for He* as well as for He** states and 0.4–19% for He$^+$ states; however, for most of these states, the discrepancy is below 1%. Note

TABLE I

$\mu^z(t)$, $N_w(t)$, $\{[N_w(t)] / [N(t)]\} \times 100$ and $|\langle \Psi(0)|\Psi(t)\rangle|^2$ for a He atom under an intense laser field; all values are in atomic units [see Eqs. (19), (24), and (25)].

t	$\mu^z(t)$	$N_w(t)$	$\dfrac{N_w(t)}{N(t)} \times 100$	$|\langle \Psi(0)|\Psi(t)\rangle|^2$
0.016839	0.111318E-08	1.96517	98.29044	0.9954139
0.210488	0.1239609E-06	1.96241	98.15161	0.9632689
11.61896	0.3630145E-05	1.60932	80.45920	0.7042549
24.24827	−0.2352783E-05	1.40847	70.61764	0.6378755
36.87758	−0.181487E-04	1.05833	53.08885	0.5724478
49.50689	0.153491E-04	1.58046	79.31107	0.6659942
62.13620	0.4417561E-04	1.51885	76.44839	0.6671913
74.7655	0.2563478E-05	1.60945	80.82953	0.7023679
93.70947	−0.1900946E-03	1.57698	79.47659	0.5719749
112.6534	0.2909862E-02	1.57105	79.80110	0.7231097
131.5974	−0.4093559E-01	1.26046	63.48783	0.4309069
150.5414	0.2315859E-01	1.53306	78.26805	0.6623417
169.4853	−0.2485412E-01	1.32505	67.59104	0.4395858
188.4293	−0.1397026	1.33865	68.87593	0.5724217
207.3732	0.4463731	1.22307	62.51277	0.3771261
220.0025	−0.375423	1.13847	58.68950	0.3294173
222.5284	−0.1423769	1.37425	71.60154	0.5344772
225.0543	−0.8062962	1.39046	72.42507	0.5828086
227.8327	−0.162543	1.14457	59.68453	0.5096819
246.7767	−0.2275418	1.42399	74.88587	0.6196147
265.7206	0.3409082	1.25566	66.09681	0.4826942
284.6646	−0.1067838	1.36684	72.25689	0.5972677
303.6086	−0.4516896	1.07166	56.62362	0.3071347
322.5525	−0.1255609	1.15875	62.16312	0.5302418
341.4965	0.1024642	1.29635	69.24957	0.4822863
360.4404	0.3719385	0.94306	50.63902	0.3412317
379.3844	0.6069082	1.20624	65.72034	0.5161579
398.3284	0.6441741	1.47282	80.01568	0.5128579
417.2723	−0.5374177E-01	1.33814	73.67771	0.5768151
436.2163	−0.7864991	1.42681	79.09355	0.5260086
455.1602	−0.6108469	1.21669	67.68466	0.3777132
474.1042	0.8927948	1.38865	77.55177	0.3698736
493.0482	−0.8614756	0.96879	54.67849	0.3500375
511.9921	0.7062094	1.39529	78.50825	0.2906393
530.9361	−0.4718247	0.72019	40.94860	0.3213105
549.8801	−0.7179571	1.22589	70.73952	0.3282773
568.824	0.4887033E-01	0.93359	54.15737	0.3361956
587.768	1.182094	1.31247	76.09819	0.3690087
606.712	0.54322	0.97940	56.88826	0.3156804
625.6559	−0.3792753	1.25320	73.84943	0.4131645
644.5999	1.170212	1.00008	59.33808	0.3276103
663.5438	0.1046965	0.88124	52.41236	0.1785025
682.4878	0.764809E-01	0.92934	55.90329	0.2558469
701.4318	0.2677905	0.74133	44.87508	0.2596583
720.3757	−0.6602697	1.25723	76.20416	0.3205976
739.3197	−0.1840865	0.56474	34.31731	0.2297366
750.4335	−0.8865657E-01	0.89375	54.63207	0.2647704
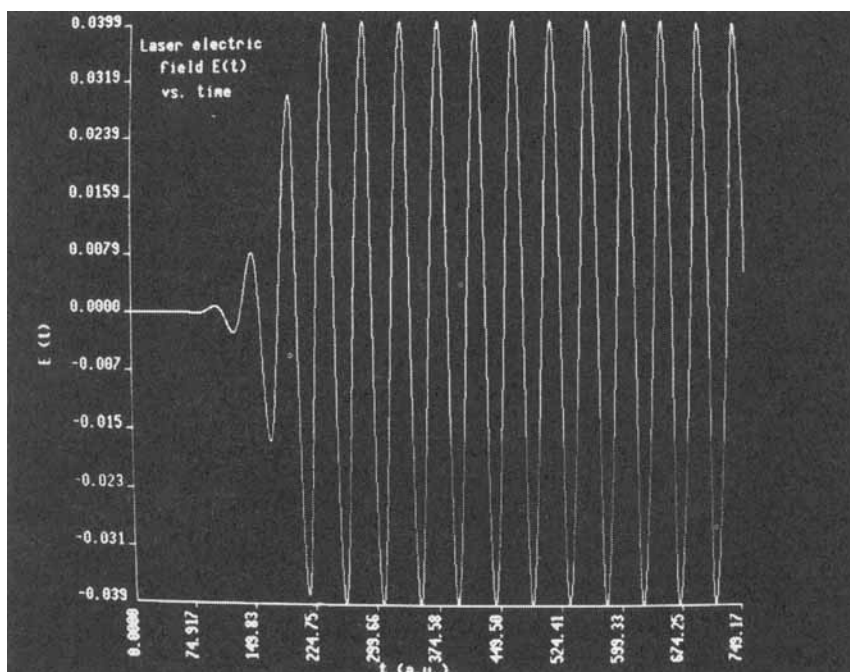
FIGURE 4. Plot of rapidly oscillating excitation and ionization probability against time, in au. Here, $S(t)$ is the same as $p_{ei}(t)$ in Eq. (23).
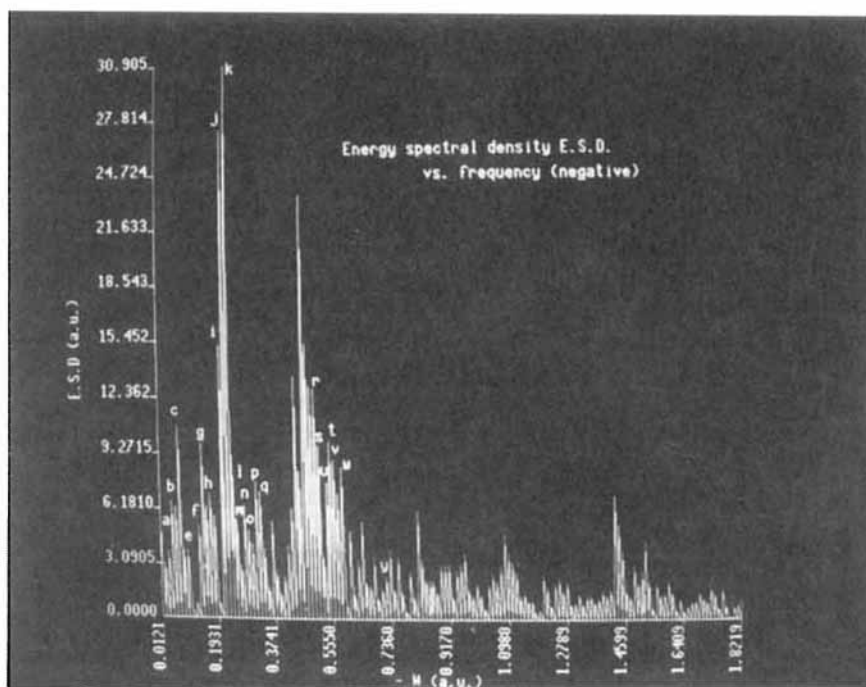
FIGURE 5. The energy spectral density, ESD(ω), plotted against negative values of ω, in au. The continuum range (ω positive) is not shown. The peaks labeled as a, b, c, j, and r correspond to He$^+$ states with $n = 13, 7, 5, 3$ and 2, respectively. All the other labeled peaks correspond to doubly excited (autoionizing) states of He. See Tables II–V.

TABLE II
Singly excited singlet and triplet He states in the energy spectrum (Fig. 5) at $t = 517.29647$ au; all values are in atomic units; in column 2, the reference values for comparison are taken from [50] [see Eq. (28)].

State	$-E$ (reference value)	$-E$ (present value)	ESD	$\dfrac{\text{ESD}}{\text{TSD}} \times 100$
$1s^2(1^1S)$	2.903490	2.902941	0.5485	0.6005E-02
$1s2s(2^3S)$	2.175629	2.174169	0.7588	0.8307E-02
$1s2s(2^1S)$	2.146371	2.149877	0.7556	0.8272E-02
$1s2p(2^3P)$	2.133598	2.137731	0.5801	0.6351E-02
$1s2p(2^1P)$	2.124239	2.125585	0.7929	0.8681E-02
$1s3s(3^3S)$ ⎫	2.069099	2.064853	0.5916	0.6477E-02
$1s3s(3^1S)$ ⎭	2.061680			
$1s3p(3^3P)$ ⎫	2.058492	2.052707	0.7533	0.8247E-02
$1s3p(3^1P)$ ⎭	2.055555			
$1s4s(4^3S)$	2.036925	2.040561	1.0795	0.1182E-01
$1s5s(5^3S)$	2.023033	2.028415	1.1772	0.1289E-01
$1s6p(6^3P)$	2.014623	2.016269	0.4793	0.5247E-02
$1s10s(10^3S)$	2.005726	2.004122	0.5966	0.6532E-02

also the presence of both singlet and triplet He* as well as He** states. Thus, a spin-off from the present work is the calculation of excited-state energies. However, in Figure 5, many peaks, especially those between q and r as well as those to the right of y, have not been identified. These do not seem to correspond to known states of He and He$^+$. One might speculate on their being Stark-shifted He** and He$^+$ states as well as Rydberg states.

Based on the ESD analysis for $t = 517.29647$ au, in particular, the magnitude and percent contribution of the ESD to the TSD, the role of route a [see (iv) in the method of calculation section] in the overall interaction process is least significant at this time. Since the largest ESD values come from He** and continuum states, both sequential ionization (SI) and ATI are significant. The autoionizing (resonance) He** states decay nonradiatively to He$^+$ according to route d. Thus, routes b, c, d, and e occur dominantly. However, the excitation routes f–i cannot be ruled out, while route j completes the SI. Photoemissions from He*, He**, He$^+$*, and continuum states also occur [46]. Note that the complexion of the energy spectrum and the relative significance of the various states will change in the course of time, depending on the intensity and duration of the laser pulse.

The calculated average photoionization rate (R) and total photoionization cross section (σ_{ion}), given by Eqs. (30) and (31), are 2.014474×10^{13} s^{-1} and 1.5683×10^{-18} cm^2, respectively. These values

compare well with Kulander's [5] TDHF calculations which used lasers of different frequency, intensity, and pulse duration from the laser employed here.

The nature and geometry of the density and potential oscillations due to the atom–laser interaction are vividly realized through computer visualizations of TD $\Delta\rho(\bar{p}, \bar{z}, t)$ and $\Delta V_{eff}(\bar{p}, \bar{z}, t)$ [Eqs. (20) and (21)]. Figures 6 and 7 depict these quantities, respectively, projected onto the ($\bar{p}, \bar{z}$) plane at different time steps. In Figure 6, the white region (He nucleus at its center) and the halo surrounding it correspond to negative $\Delta\rho$, while the other areas correspond to positive $\Delta\rho$. First, note the distorted p-orbital shape of the negative region (NR) in Figure 6. The electronic charge is depleted in regions near the nucleus and increased along the $\bar{z}$ and $\bar{p}$ directions. The entire NR oscillates nonlinearly and changes its shape along these two directions. While the patterns are symmetrical in $\bar{p}$, the asymmetry with respect to $\bar{z}$ oscillates from left to right faster than does the switching of direction of the laser field. The outer part of the NR is more polarized (distorted) than is the inner part. Note the *onionlike layered structure* of the NR which always remains enclosed within the window.

Consider now the positive regions (PR) of $\Delta\rho$ in Figure 6. The extremely interesting geometrical dispositions of the PR need a detailed topographical analysis which has not been attempted in this study and remains a subject for future investigation. The PR is concentrated along both $\bar{z}$ and $\bar{p}$,

TABLE III

Doubly excited singlet and triplet states of He in the energy spectrum (Fig. 5) at t = 517.29647 au; all values are in atomic units [see Eq. (28)].

State	$-E$ (reference value)	$-E$ (present value)	ESD	$\dfrac{\text{ESD}}{\text{TSD}} \times 100$	Label in Figure 5
$2s^2(^1S)$	0.77675[a]	0.777357	0.4060	0.4445E-02	—
$2s2p(^3P)$	0.76051[a]	0.765210	1.5500	0.1697E-01	—
$2p^2(^3P)$	0.71044[a]	0.716626	2.4337	0.2664E-01	y
$2p^2(^1D)$	0.70288[a]	0.704480	1.7618	0.1929E-01	—
$2s2p(^1P)$	0.69388[a]	0.692333	1.1376	0.1246E-01	—
$2s3s(^1S)$	0.59006[a]	0.595164	0.7971	0.8727E-02	—
$2p3p(^3D)$	0.58381[a]	0.583018	8.4685	0.9272E-01	w
$2p3p(^1P)$	0.58017[a]	0.570871	6.9912	0.7654E-01	—
$2s3d(^3D)$	0.55929[b]	0.558725	8.9005	0.9744E-01	w
$2s4s(^1S)$ $\Big\rbrace$	0.54339[a]	0.546579	9.9379	0.1088	t
$2p4p(^3D)$	0.54214[a]				
$2p4p(^1D)$ $\Big\rbrace$	0.53714[a]	0.534433	7.6539	0.8380E-01	u
$2s4d(^3D)$	0.53319[b]				
$2s5s(^1S)$ $\Big\rbrace$	0.52699[c]	0.522287	3.4681	0.3797E-01	—
$2p5d(^3F)$	0.52189[b]				
$26sp(+)(^1P)$	0.51476[a]	0.510140	9.6793	0.1060	s
$3s3s(^1S)$	0.35199[c]	0.352240	1.7895	0.1959E-01	—
$3p3p(^1D)$	0.32849[c]	0.327947	7.1562	0.7835E-01	q
$3d3d(^1G)$	0.31179[c]	0.315801	7.7148	0.8446E-01	p
$3s4s(^1S)$	0.28829[c]	0.291509	4.9915	0.5465E-01	o
$3s5s(^1S)$	0.27019[c]	0.279363	6.3933	0.6999E-01	n
$3d5d(^1G)$	0.26649[c]	0.267216	3.0896	0.3383E-01	—
$35sd(-)(^3D)$	0.25599[b]	0.255070	5.5881	0.6118E-01	m
$35sp(+)(^1P)$	0.24986[a]	0.242924	9.1341	0.1000	l
$37sp(+)(^1P)$	0.23498[a]	0.230778	30.9051	0.3384	k
$4s4s(^1S)$	0.20529[c]	0.206485	15.2498	0.1670	i
$4s4p(^1P)$	0.19279[a]	0.194339	0.8401	0.9197E-02	—
$4s5s(^1S)$	0.17679[c]	0.170047	7.0189	0.7684E-01	h
$45sd(+)(^3D)$	0.15939[b]	0.157901	6.3187	0.6918E-01	—
$5s5s(^1S)$	0.14029[c]	0.145754	9.7745	0.1070	g
$5p5p(^1D)$	0.13629[c]	0.133608	5.2155	0.5710E-01	f
$5s5p(^3D)$	0.09639[b]	0.097170	3.9126	0.4280E-01	e
$5p5d(^3F)$	0.08299[b]	0.085023	3.8649	0.4230E-01	—

[a] Taken from [51].
[b] Taken from [52].
[c] Taken from [53].

mostly well outside the NR. However, in the course of rapid oscillations, the PR penetrates fairly close to the nucleus along the $\bar{z}$-axis. Up to t = 227.8 au, when the Gaussian pulse function has reached its peak value of unity, the PR is almost symmetric in $\bar{z}$ (like the NR, the PR is always symmetrical in $\bar{\rho}$). Beyond this time, the left–right asymmetry of the PR and its left–right switching is quite dramatic. The PR gradually and oscillatingly builds up along the $\bar{z}$-axis and oozes out of the computation grid

along the $\bar{z}$-direction in fits and bursts. Thus, while the PR oscillates in and out of the window, acquiring birdlike, dragonflylike, etc., shapes, it hardly ever touches the grid periphery along the $\bar{\rho}$-direction. For example, along the $\bar{\rho}$ direction, the PR is outside the window at t = 36.88 au, but, inside, it is at t = 62.14 au.

In Figure 7, the onionlike NR in ΔV_{eff} covers a larger part than does the PR in the computation grid. The PR touches the grid periphery in both $\bar{\rho}$

TABLE IV

He$^+$ states in the energy spectrum (Fig. 5) at t = 517.29647 au; all values are in au; reference values in column 2 are obtained from the relation, $-E = (Z^2/n^2)R_{He^+}$, R_{He^+}= 0.4999297 au.

State	$-E$ (reference value)	$-E$ (present value)	ESD	$\frac{ESD}{TSD} \times 100$	Label in Figure 5
He$^+$ (n = 1)	1.99972	1.991976	1.1206	0.0123	—
He$^+$ (n = 2)	0.49993	0.497994	12.7570	0.1397	r
He$^+$ (n = 3)	0.22219	0.218632	27.2114	0.2980	j
He$^+$ (n = 4)	0.12498	0.121462	0.9148	0.0100	—
He$^+$ (n = 5)	0.07999	0.072877	10.7855	0.1181	c
He$^+$ (n = 6)	0.05555	0.060731	6.3166	0.0692	—
He$^+$ (n = 7)	0.04081	0.048585	6.5918	0.0722	b
He$^+$ (n = 9)	0.02469	0.024292	3.1309	0.0343	—
He$^+$ (n = 13)	0.01183	0.012146	5.5143	0.0604	a

and $\tilde{z}$ directions. Comparing Figures 6 and 7, it is observed that the PR in $\Delta\rho$ tends to lie mostly in the lighter areas of NR in ΔV_{eff}. The PR in ΔV_{eff} does not appear to be simply related to the PR in $\Delta\rho$. Overall, ΔV_{eff} is more spread out than is $\Delta\rho$. However, the core of the NR in the former has the same distorted p-orbital-like structure as in the latter.

Conclusion

The present TDQM calculations on the He atom under an intense laser field, using the hydrodynamical GNLSE approach based on densities, lead to the following conclusions:

1. The essential physical features corresponding to multiphoton ionization and photoemission [46] can be understood in an integrated manner. MPI occurs in both sequential and above-threshold modes. Excitation occurs faster than does ionization, which occurs in fits and bursts. Various routes for excitation and ionization have been identified, each route involving many states.

2. Vigorous, nonlinear, space–time oscillations of periods faster than that of the laser field are observed with the density, difference density, effective potential surface, excitation and ionization probability, total electronic charge, dipole moment, etc. This indicates nonresonant adsorption. The TD dipole moment contains the footprint of quantum chaos [36].

3. The time-evolved density is a mixture of

densities from a large number of excited and ionized states of He, including the continuum. Using FFT, the computed energy spectrum identifies many singlet and triplet states of He* and He** as well as several states of He$^+$. The agreement of our calculated excited-state energies with experimental and other theoretical values is generally excellent. Thus, a bonus from the present TDQM approach is the calculation of excited-state energies indicating the link between time dependence and excited states.

4. There occurs a tug of war between the nucleus and the laser field for the electron density, which the nucleus gradually loses. Electron density is depleted from regions near the nucleus and built up elsewhere, but a part of the density keeps returning to regions fairly close to the nucleus.

5. Computer visualizations of the entire dynamical process from start to finish are effectively done through two-dimensional maps of TD $\Delta\rho$ and ΔV_{eff}. The $\Delta\rho$ maps show extremely interesting geometrical features. Both the NR and PR in $\Delta\rho$ oscillate and change shapes rapidly. The NR shows a layered onionlike structure, while the PR penetrates fairly close to the nucleus (see 4 above) along the field axis. The PR acquires birdlike, dragonflylike, etc., shapes. The NR in ΔV_{eff} is more dispersed than that in $\Delta\rho$. Both the NRs have a distorted p-orbital-like shape.

6. Although a hypothetical laser has been employed for computational economy, the results of the present calculations are

TABLE V

Continuum states of He with large contributions to the energy spectrum; many other continuum states with smaller ESD occur (see text); all values are in au.

E (present value)	ESD	$\frac{ESD}{TSD} \times 100$	E (present value)	ESD	$\frac{ESD}{TSD} \times 100$
0.085023	16.9537	0.1856	1.251058	34.2380	0.3748
0.097170	15.7144	0.1720	1.287497	25.2911	0.2769
0.121462	21.9559	0.2404	1.348228	31.1429	0.3410
0.133608	13.2342	0.1449	1.360374	25.4125	0.2782
0.145754	14.7857	0.1619	1.396813	26.0588	0.2853
0.230778	15.4274	0.1689	1.421105	36.3453	0.3980
0.267216	34.1666	0.3741	1.433251	38.5769	0.4224
0.279363	55.7819	0.6107	1.445397	45.2455	0.4954
0.340094	10.2322	0.1120	1.457544	30.0703	0.3292
0.485848	12.0428	0.1319	1.469690	27.5360	0.3015
0.825941	29.1797	0.3195	1.481836	50.3733	0.5515
0.862380	80.3564	0.8798	1.493982	3.3987	0.0372
0.886672	110.1545	1.2060	1.506128	34.9818	0.3830
0.898819	211.7414	2.3182	1.518275	23.9231	0.2619
0.910965	261.6610	2.8647	1.566859	36.6839	0.4016
0.923111	165.1806	1.8084	1.591152	33.0216	0.3615
0.935257	81.8084	0.8957	1.615444	20.0613	0.2196
0.947403	188.1913	2.0604	1.651883	31.7153	0.3472
0.959550	178.3319	1.9524	1.676175	34.0045	0.3723
0.971696	99.3812	1.0881	1.688321	24.8201	0.2717
0.983842	280.2291	3.0680	1.736906	15.5360	0.1701
0.995988	193.0562	2.1136	1.858368	11.2073	0.1227
1.008134	173.9237	1.9042	1.882661	15.0039	0.1643
1.020281	156.7669	1.7163	1.919099	15.3773	0.1684
1.044573	83.3682	0.9127	1.991976	17.5008	0.1916
1.056719	80.3669	0.8799	2.077000	10.5700	0.1157
1.068865	89.8264	0.9834	2.137731	7.1869	0.0787
1.081012	81.3077	0.8902	2.247046	6.0399	0.0661
1.093158	74.6691	0.8175	2.380655	7.6263	0.8349
1.105304	50.8065	0.5562	2.660017	4.3872	0.0480
1.117450	68.7238	0.7524	2.732894	2.8352	0.0310
1.129596	65.7421	0.7198	2.878649	3.4306	0.0376
1.166035	35.4229	0.3878	3.230888	1.1547	0.0127
1.214620	35.0328	0.3835	3.267327	1.4742	0.0161
1.226766	27.1597	0.2974			

consistent with current experimental and theoretical results on photoionization and photoemission.

7. To the best of our knowledge, this may be the first instance where the hydrodynamical analogy to QM has made detailed contact with experiment. The correctness of the present results strongly emphasizes the validity of the hydrodynamical approach which leads to nonlinear equations in terms of single-particle densities.

In passing, the present approach has the potential of taking density functional theory into the quantum theory of molecular reaction dynamics.
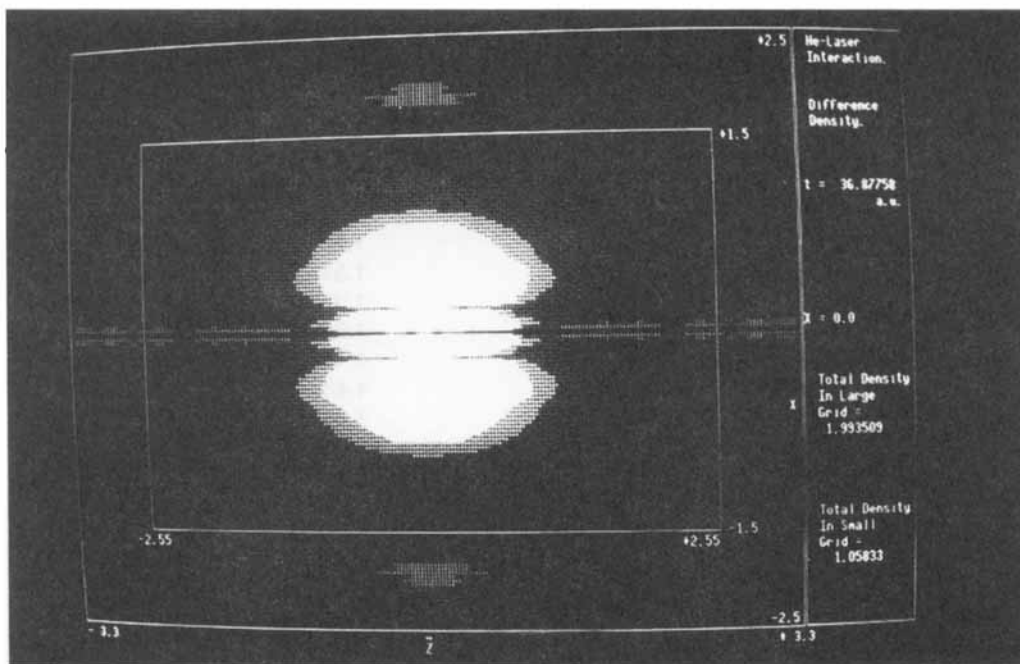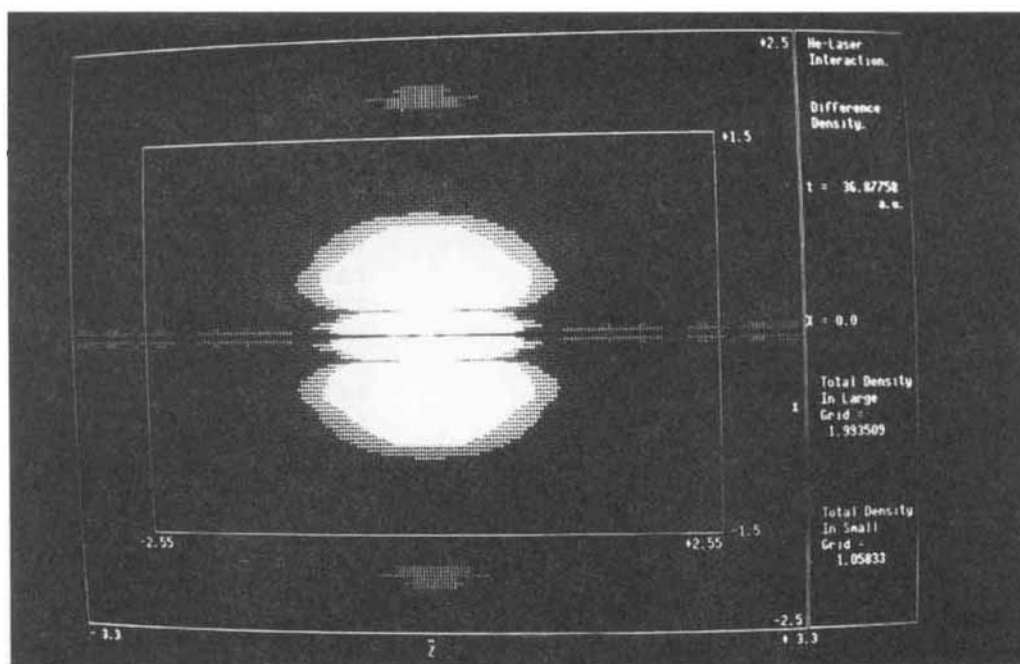
(a)
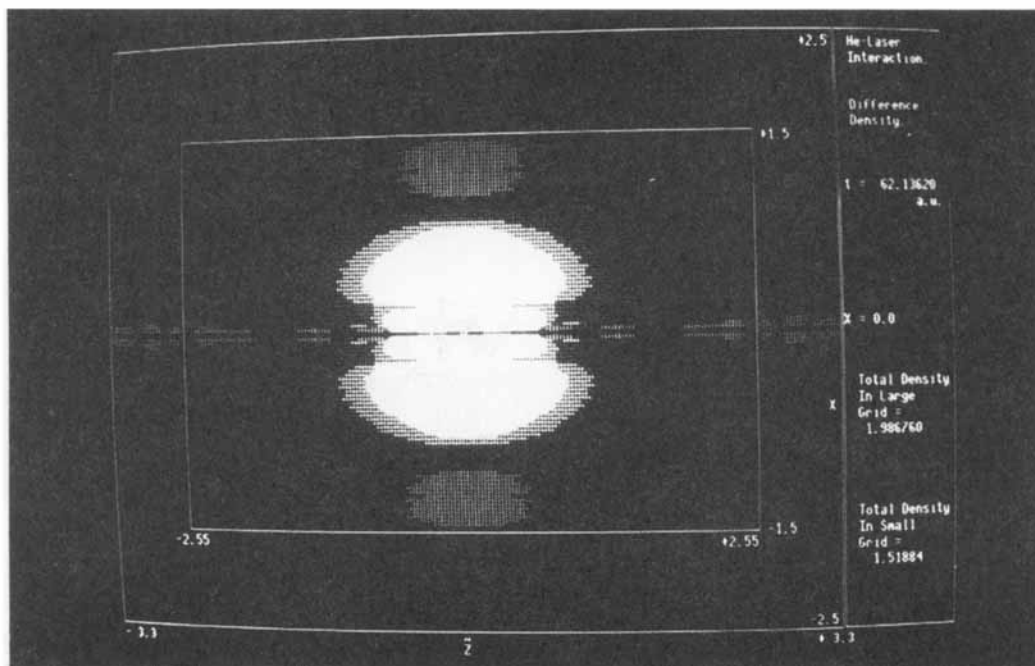
(b)

FIGURE 6. Projected difference density, $\Delta\rho(\bar{\rho}, \bar{z}, t)$, maps in the $(\bar{\rho}, \bar{z})$ plane. Both the computation grid and the window are shown. The central white region (He nucleus at its center) and the halo surrounding it correspond to negative $\Delta\rho$, while the other parts indicate positive $\Delta\rho$. The negative part is denoted by dots, while the positive part is denoted by lines. (a) $t = 36.87758$; (b) $t = 62.13620$; (c) $t = 131.5974$; (d) $t = 150.5414$; (e) $t = 169.4853$; (f) $t = 227.8327$; (g) $t = 303.6006$; (h) $t = 436.2163$; (i) $t = 474.1042$; (j) $t = 511.9921$; (k) $t = 644.5999$; (l) $t = 739.3197$; (m) $t = 750.4335$ au. Note the touching of the grid boundary and penetration fairly close to the nucleus by positive $\Delta\rho$.

(a)
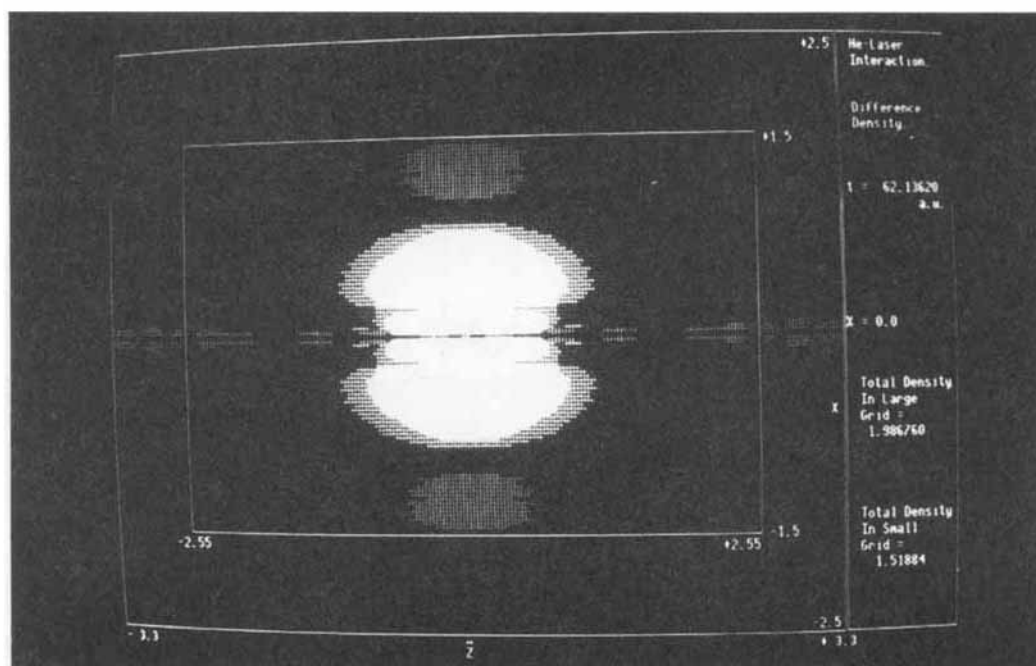
FIGURE 6. (Continued)
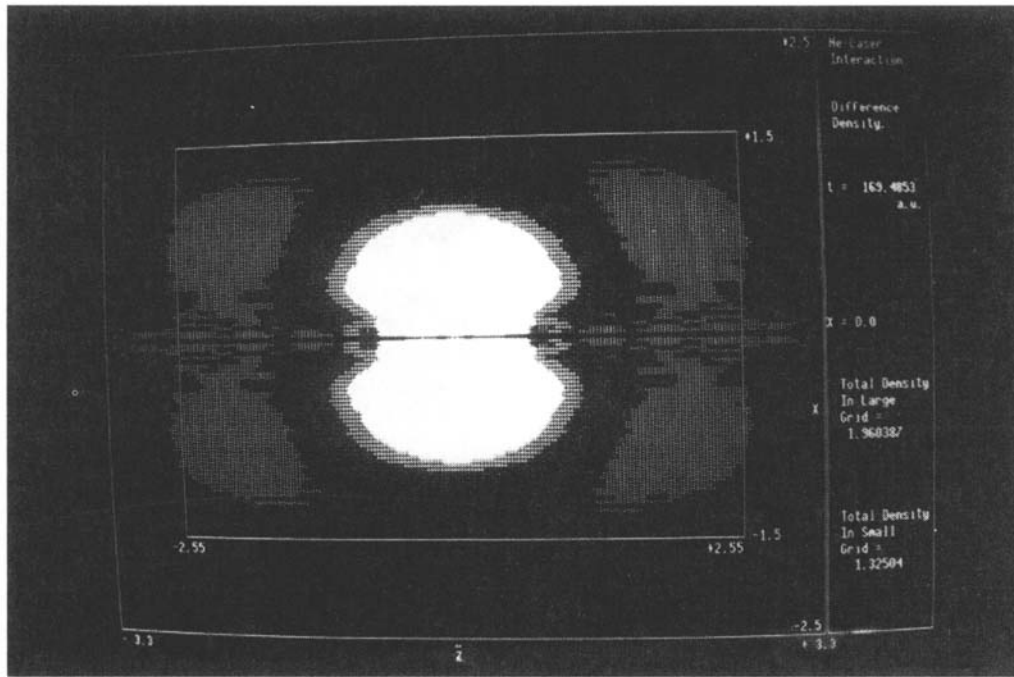
(e)
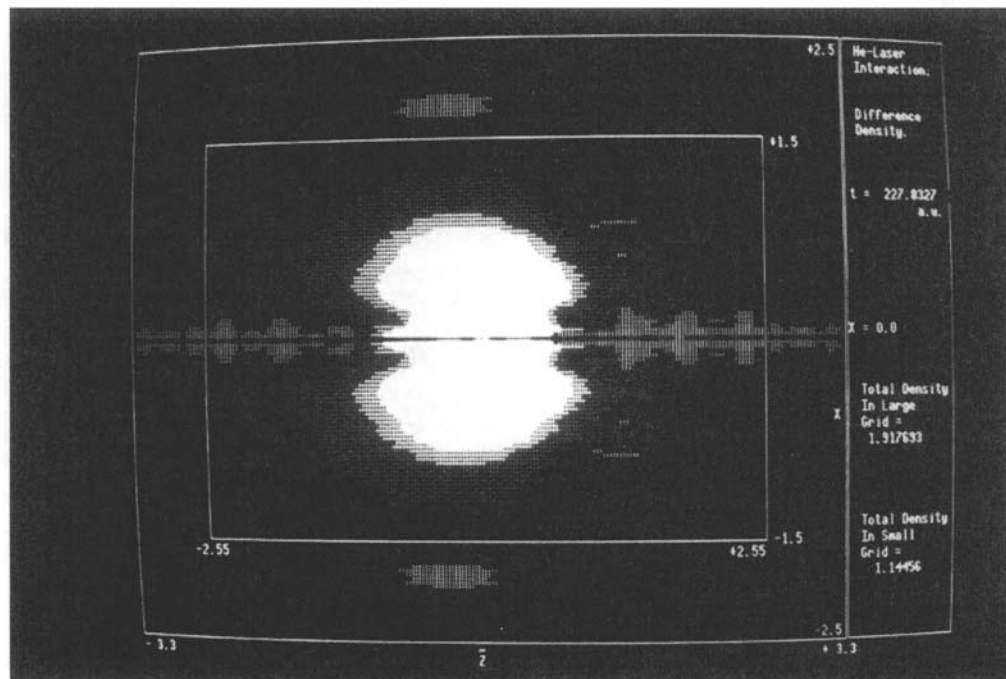
(f)

FIGURE 6. (Continued)
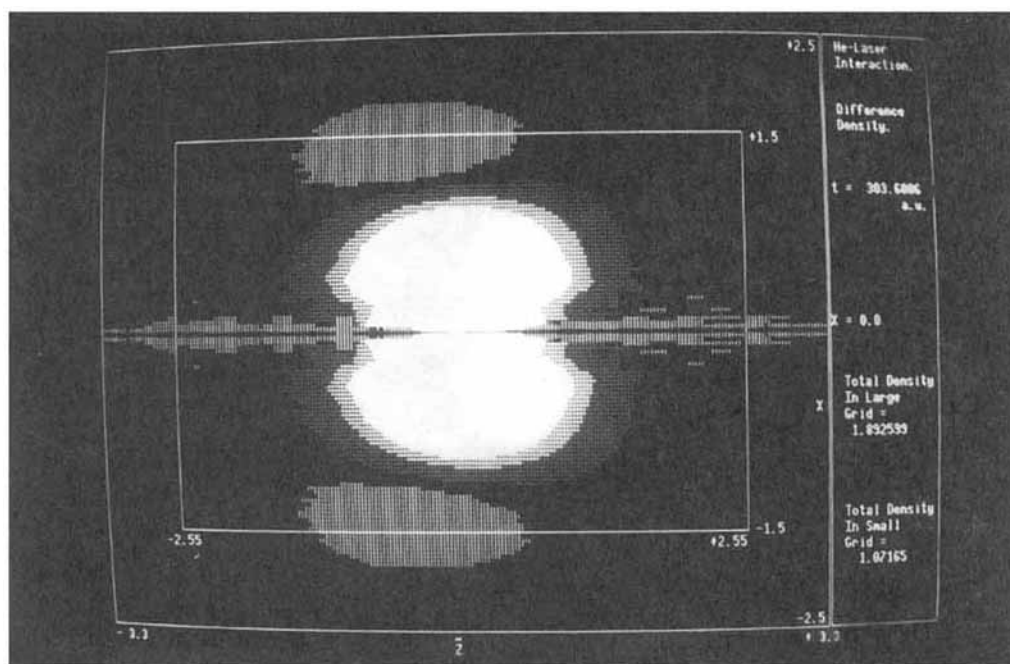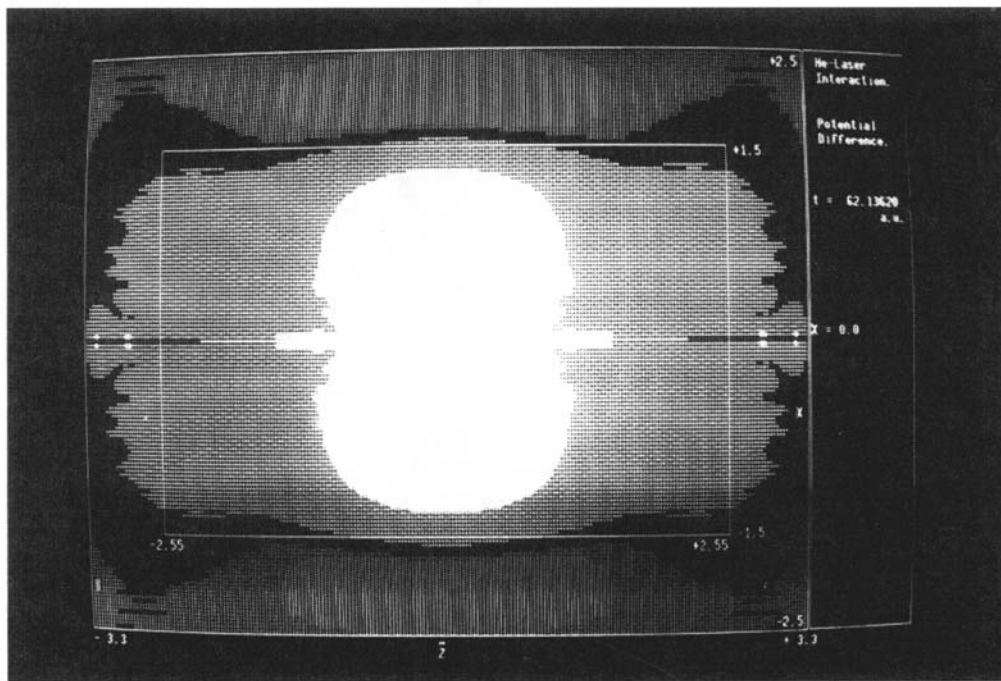
(g)
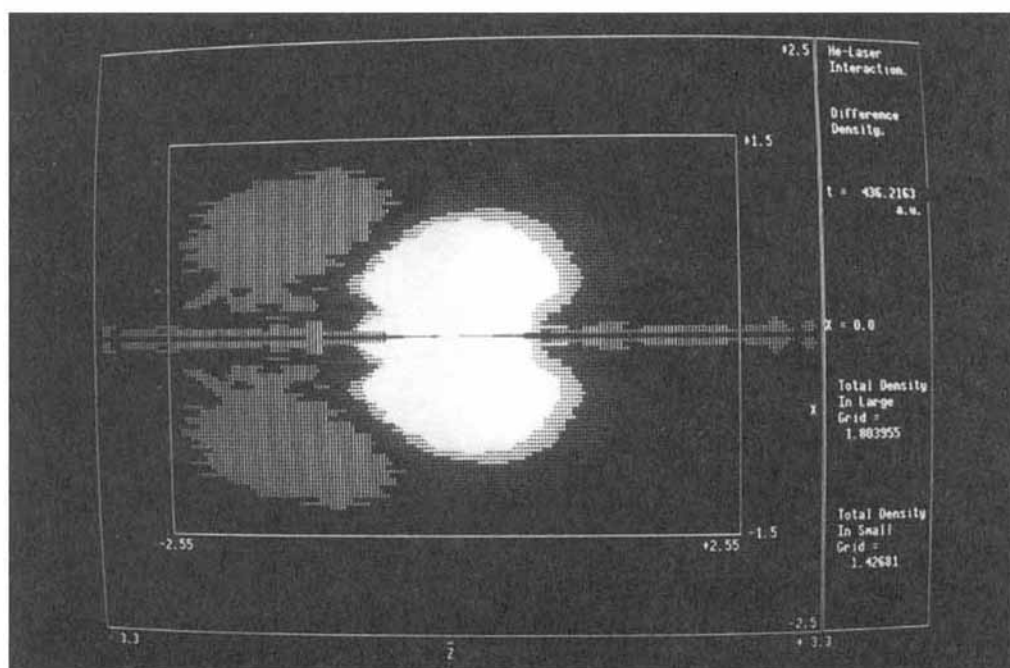
FIGURE 6. (Continued)

(i)

(j)
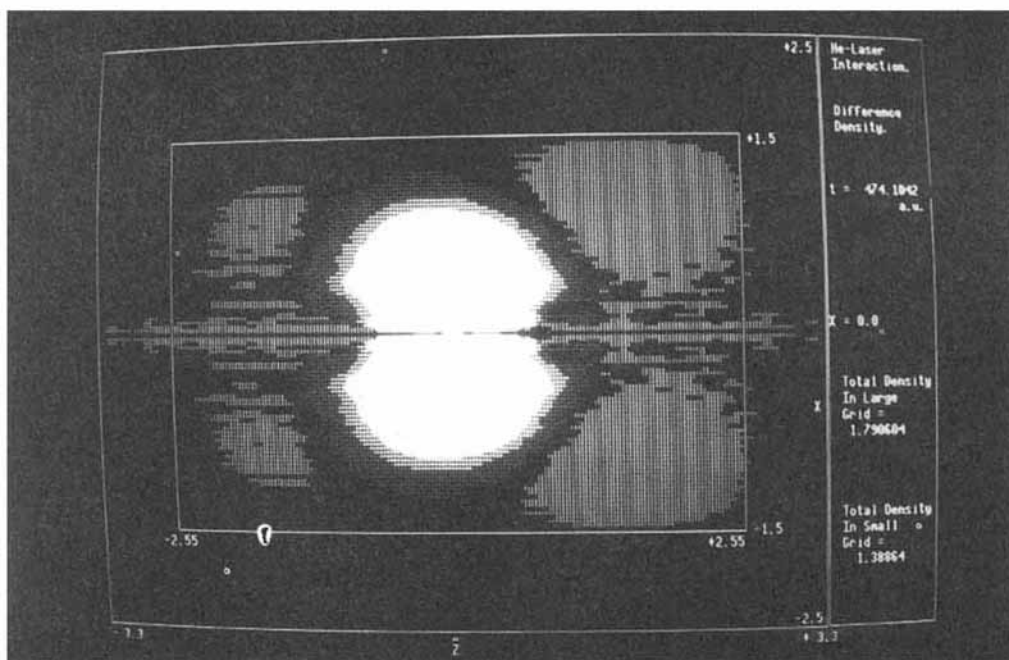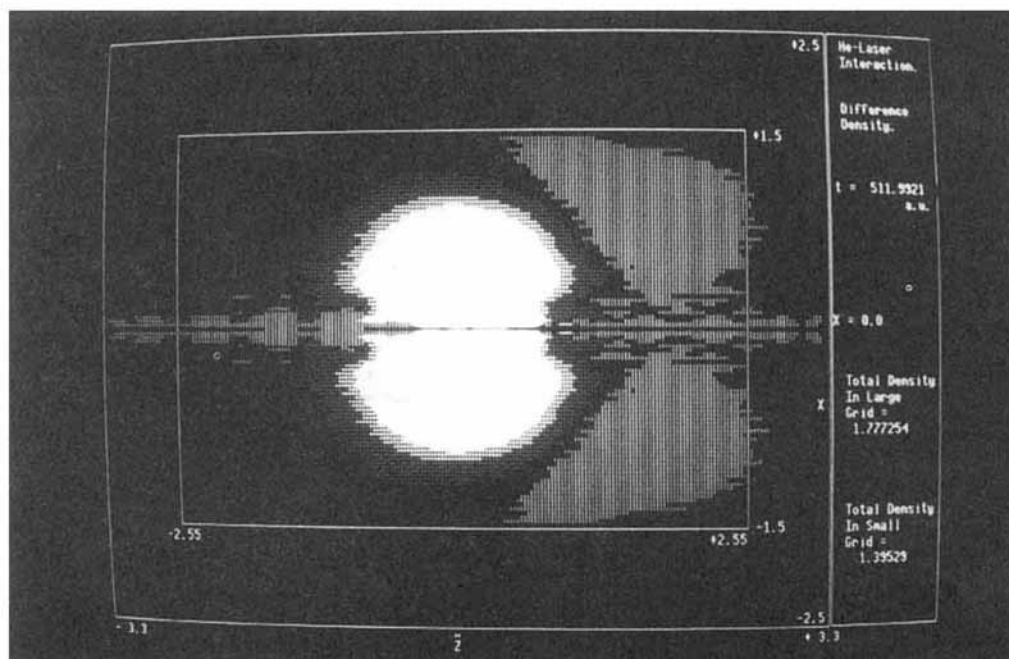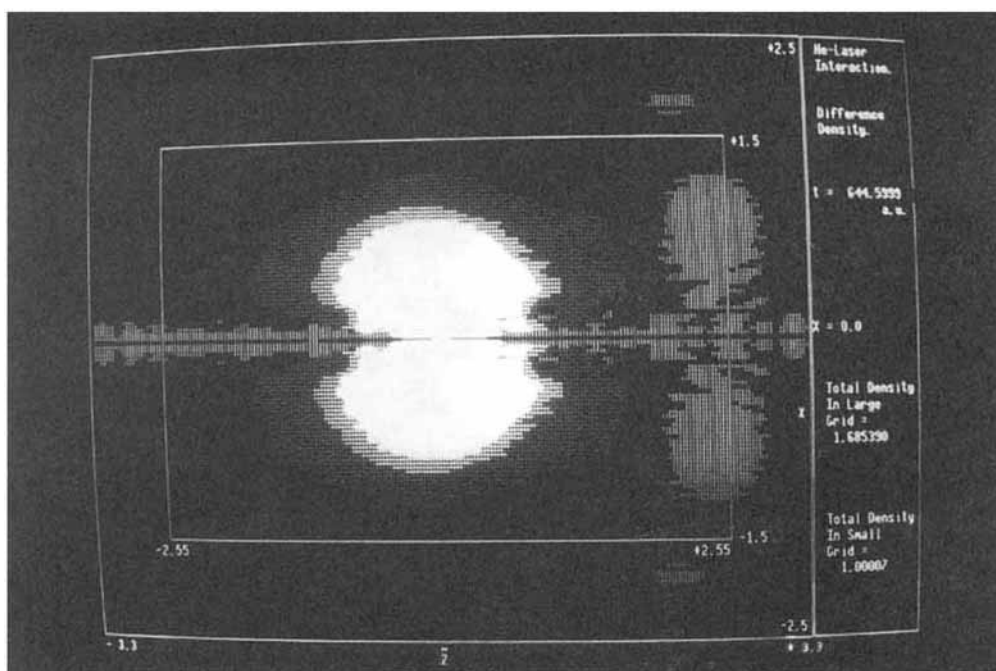
FIGURE 6. (Continued)

(k)
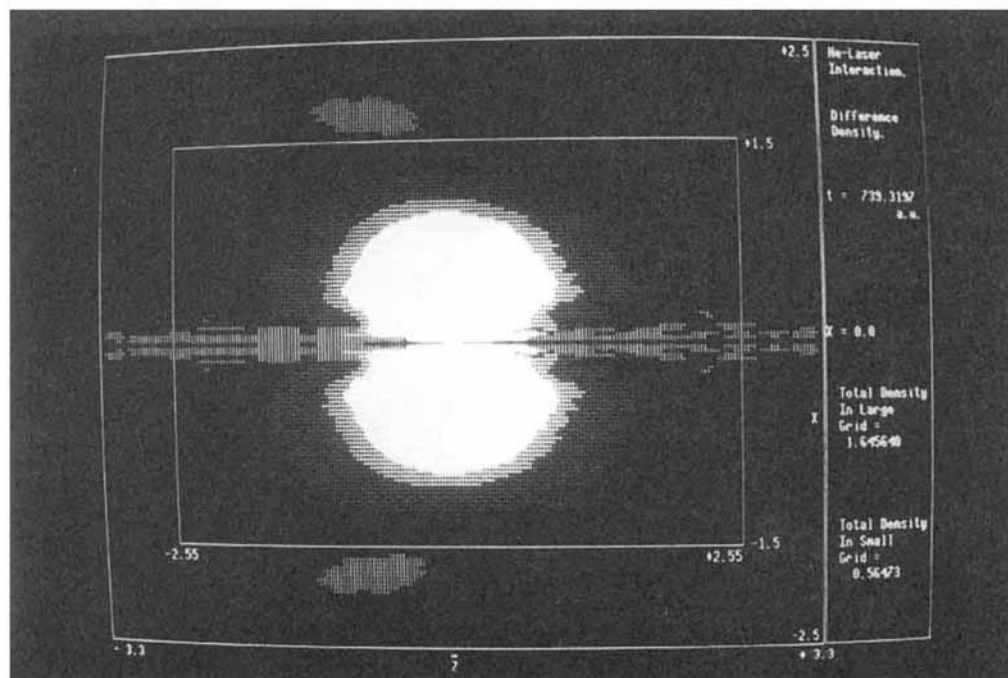
(l)

FIGURE 6. (Continued)
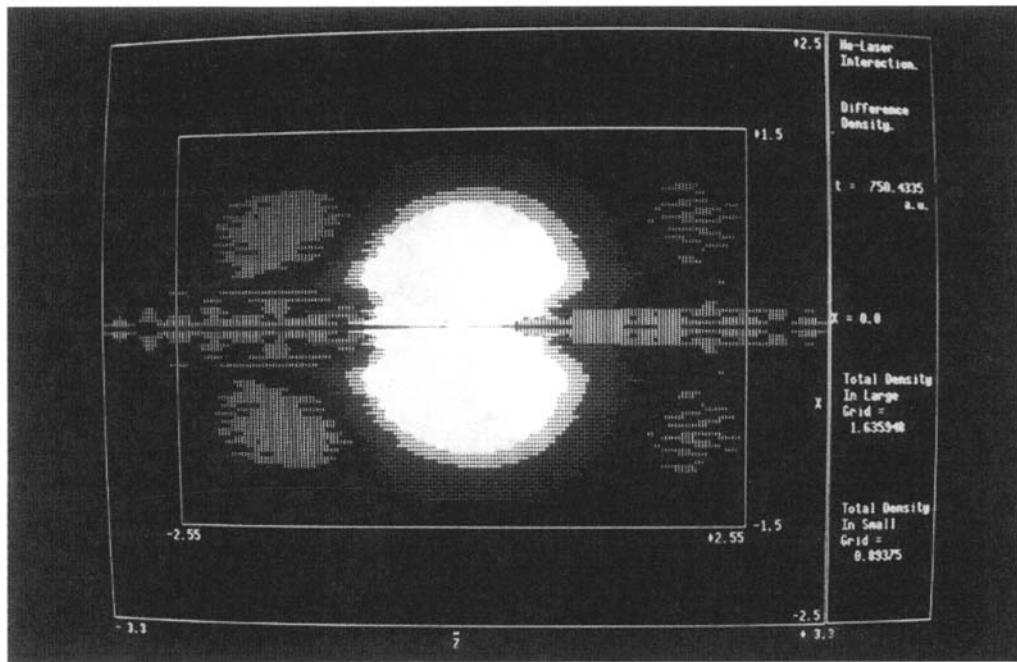
(m)

FIGURE 6. (Continued)

(a)

FIGURE 7. Projected difference potential, $\Delta V_{eff}(\tilde{\rho}, \tilde{z}, t)$, maps in the $(\tilde{\rho}, \tilde{z})$ plane. Both the computation grid and window are shown. The central white region (He nucleus at its center) and the halo surrounding it correspond to negative ΔV_{eff}, while the other parts indicate positive ΔV_{eff}. The negative and positive parts are denoted by dots and lines, respectively. (a) $t = 62.13620$; (b) $t = 150.5414$; (c) $t = 169.4853$; (d) $t = 227.8327$; (e) $t = 398.3284$; (f) $t = 511.9921$; (g) $t = 750.4335$ au. See also Figure 6.
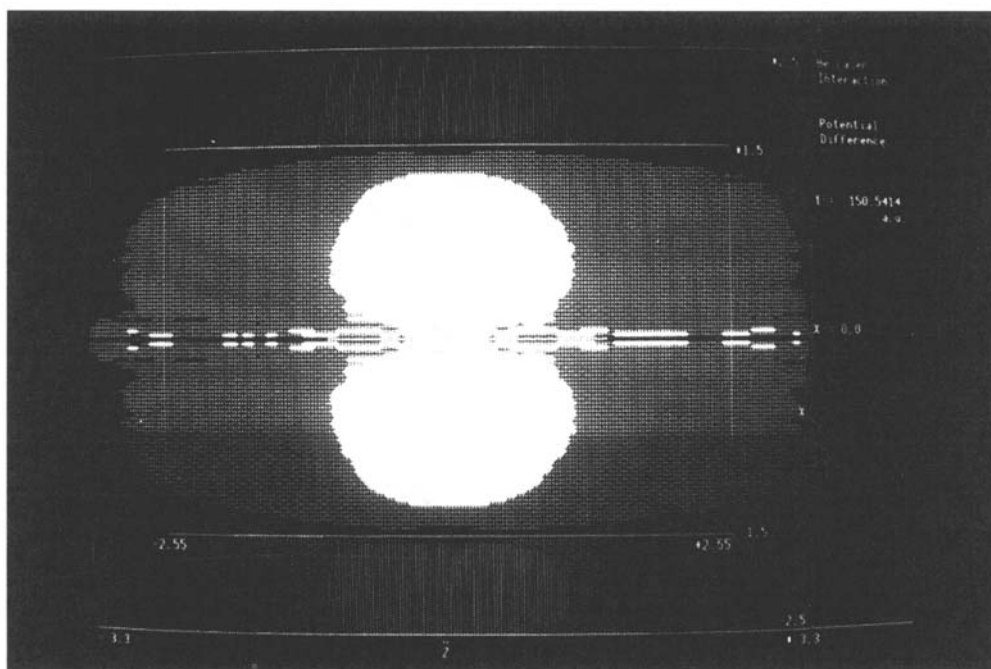
(b)
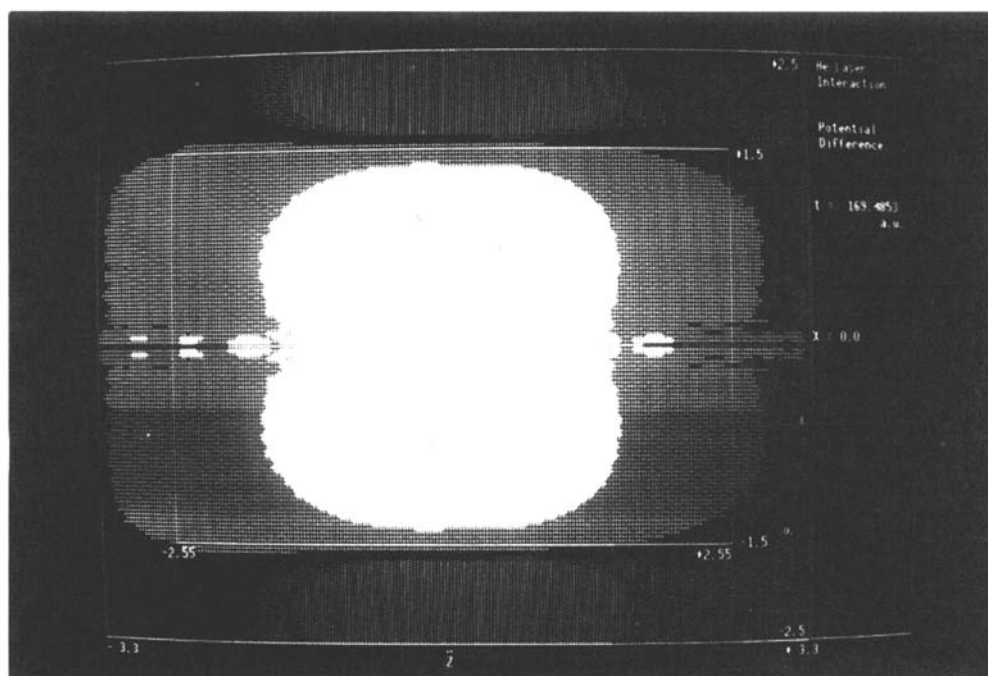
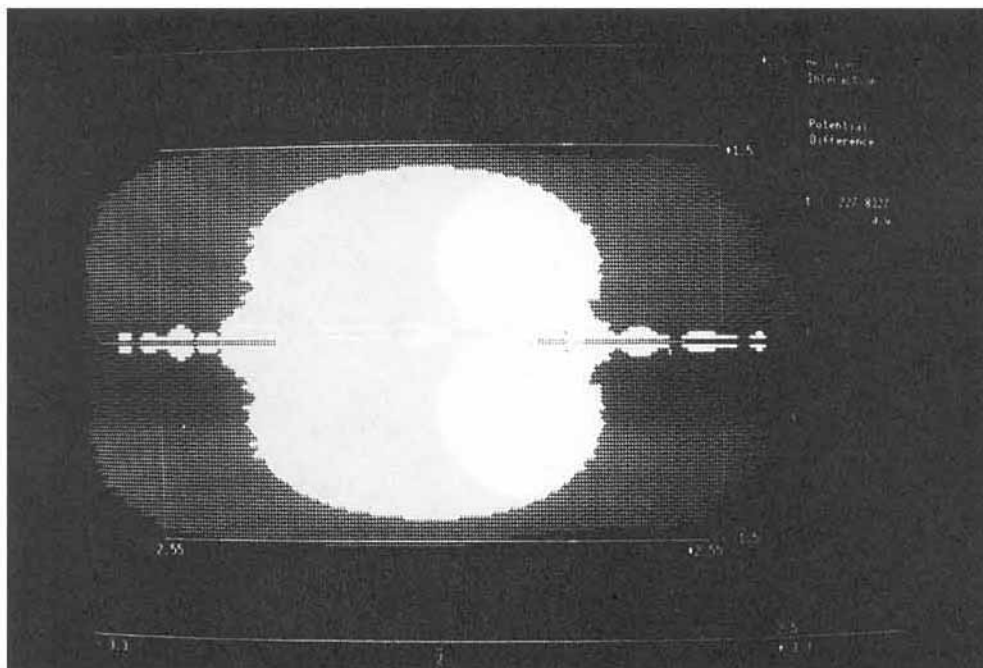
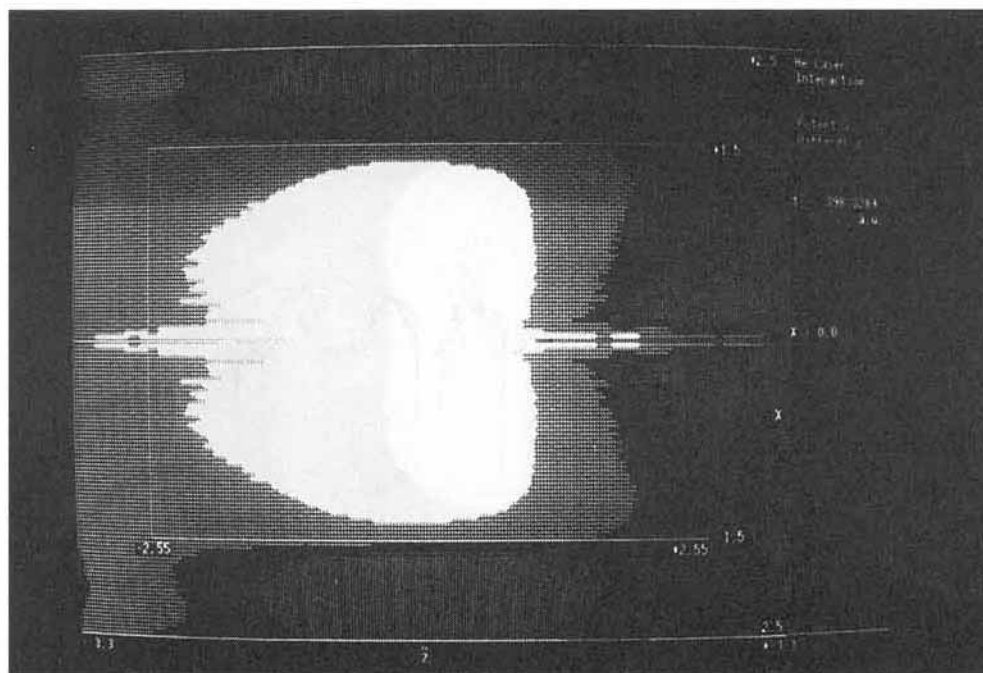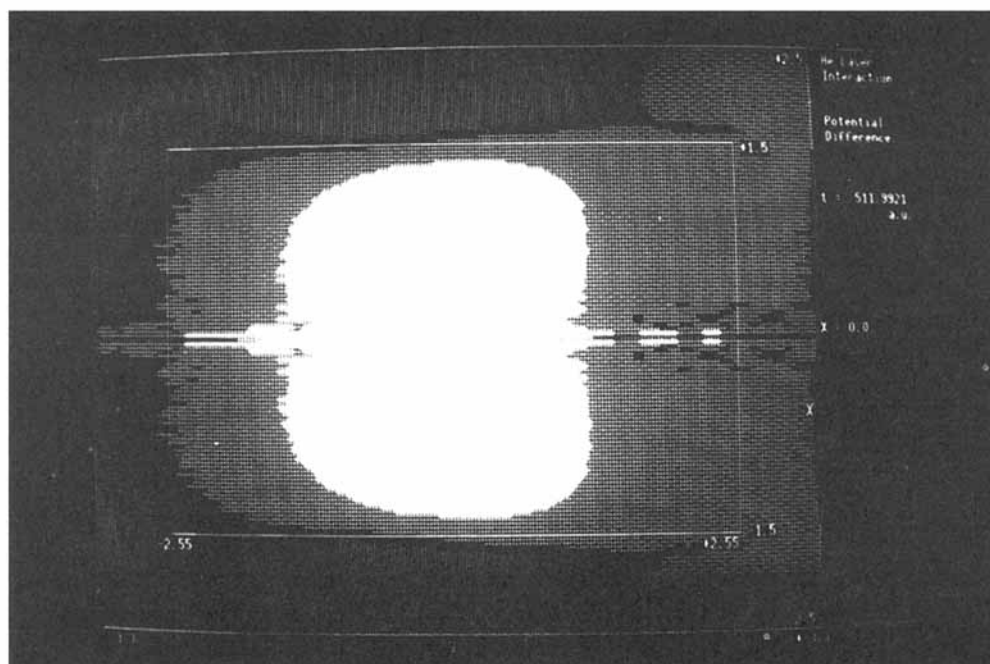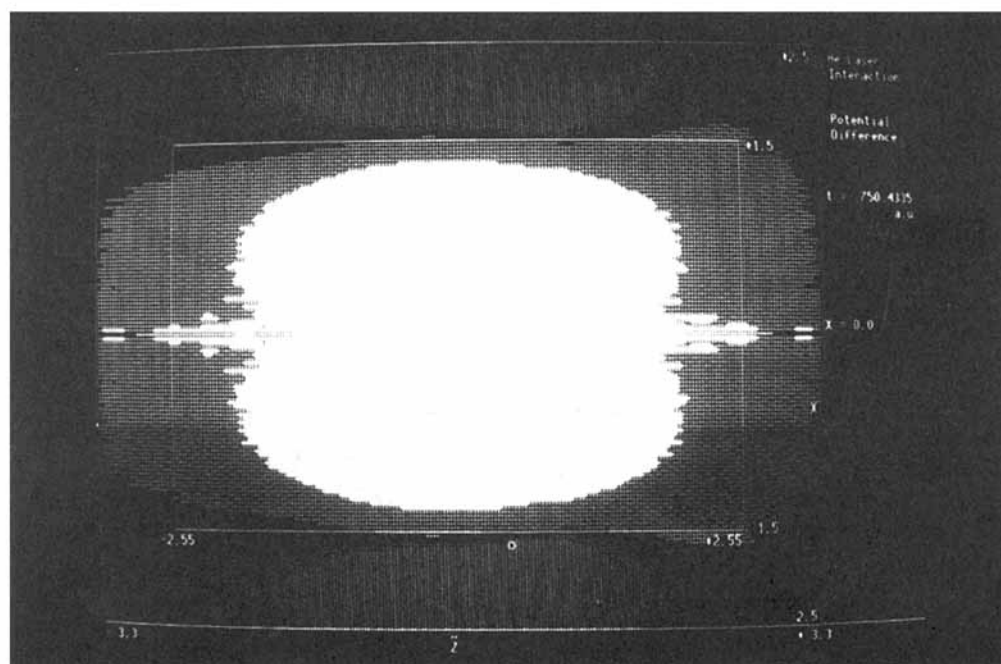
(c)

FIGURE 7. (Continued)

(d)

FIGURE 7. (Continued)

(f)

(g)

FIGURE 7. (Continued)

References

1. K. Burnett, V. C. Reed, and P. L. Knight, J. Phys. B: At. Mol. Opt. Phys. **26**, 561 (1993).
2. M. H. Mittleman, *Introduction to the Theory of Laser-Atom Interactions* (Plenum Press, New York, 1993).
3. M. Gavrila, Ed., *Atoms in Intense Laser Fields* (Academic Press, Boston, 1992).
4. B. Piraux, Ed., *Proceedings of the Workshop, Super Intense Laser Atom Physics (SILAP) III* (Plenum Press, New York, 1994).
5. K. C. Kulander, Phys. Rev. A **36**, 2726 (1987).
6. J. Javanainen, J. H. Eberly, and Q. Su, Phys. Rev. A **38**, 3430 (1988).
7. J. N. Bardsley, A. Szöke, and M. J. Comella, J. Phys. B: At. Mol. Opt. Phys. **21**, 3899 (1988).
8. J. H. Eberly, Q. Su, and J. Javanainen. Phys. Rev. Lett. **62**, 881 (1989).
9. K. C. Kulander and B. W. Shore, Phys. Rev. Lett. **62**, 524 (1989).
10. K. C. Kulander, Ed., *Time-Dependent Methods for Quantum Dynamics: A Thematic Issue of Computer Physics Communications* (North-Holland, Amsterdam, 1991).
11. J. L. Krause, K. J. Schaefer, and K. C. Kulander, Phys. Rev. Lett. **68**, 3535 (1992).
12. S. Chelkowski, T. Zuo, and A. D. Bandrauk, Phys. Rev. A **46**, R 5342 (1992).
13. V. C. Reed and K. Burnett, Phys. Rev. A **46**, 424 (1992).
14. A. L'Huillier, Ph. Balcou, S. Candel, K. J. Schafer, and K. C. Kulander, Phys. Rev. A **46**, 2778 (1992).
15. M. Lewenstein, Ph. Balcou, M. Yu. Ivanov, A. L'Huiller, and P. B. Corkum, Phys. Rev. A **49**, 2117 (1994).
16. R. M. Potvleige and R. Shakeshaft, Phys. Rev. A **40**, 3061 (1989).
17. P. B. Corkum, N. H. Burnett, and F. Brunel, Phys. Rev. Lett. **62**, 1259 (1989).
18. S. Augst, D. Strickland, D. D. Meyerhofer, S. L. Chin, and J. H. Eberly, Phys. Rev. Lett. **63**, 2212 (1989).
19. G. G. Paulus, W. Nicklich, H. Xu, P. Lambropoulos, and H. Walther, Phys. Rev. Lett. **72**, 2851 (1994).
20. K. J. Schafer, B. Yang, L. F. DiMauro, and K. C. Kulander, Phys. Rev. Lett. **70**, 1599 (1993).
21. J. Peatross, B. Buerke, and D. D. Meyerhofer, Phys. Rev. A **47**, 1517 (1993).
22. E. Mevel, P. Breger, R. Trainham, G. Petite, P. Agostini, A. Migus, J. P. Chambaret, and A. Antonetti, Phys. Rev. Lett. **70**, 406 (1993).
23. D. N. Fittinghoff, P. R. Bolton, B. Chang, and K. C. Kulander, Phys. Rev. Lett. **69**, 2642 (1992).
24. P. B. Corkum, Phys. Rev. Lett. **71**, 1994 (1993).
25. J. H. Eberly and K. C. Kulander, Science **262**, 1229 (1993).
26. A. Sanpera, Phys. Rev. A **49**, 1967 (1994).
27. K. C. Kulander, K. J. Schafer, and J. L. Krause, in *Proceedings of the Workshop, Super Intense Laser Atom Physics (SILAP) III*, B. Piraux, Ed. (Plenum Press, New York, 1994).
28. W. Becker, S. Long, and J. K. McIver, Phys. Rev. A **41**, 4112 (1990).
29. L. V. Keldysh, Zh. Eksp. Teor. Fiz. **47**, 1945 (1964): *Idem.*, Sov. Phys. JETP **20**, 1307 (1965).
30. M. Pont, N. R. Walet, M. Gavrila, and C. W. McCurdy, Phys. Rev. Lett. **61**, 939 (1988).
31. X. Tang, H. Rudolph, and P. Lambropoulos, Phys. Rev. Lett. **65**, 3269 (1990).
32. H. R. Reiss, J. Phys. B: At. Mol. Phys. **20**, L79 (1987).
33. R. V. Jensen and B. Sundaram, Phys. Rev. Lett. **65**, 1964 (1990).
34. S. K. Ghosh and B. M. Deb, Phys. Rep. **92**, 1 (1982).
35. B. M. Deb and S. K. Ghosh, in *The Single-particle Density in Physics and Chemistry*, N. H. March and B. M. Deb, Eds. (Academic Press, London, 1987).
36. Bijoy Kr. Dey and B. M. Deb, to be published.
37. R. G. Parr and W. Yang, *Density-Functional Theory of Atoms and Molecules* (Oxford University Press, New York, 1989).
38. E. S. Kryachko and E. V. Ludeña, *Energy Density Functional Theory of Many-Electron Systems* (Kluwer, Dordrecht, 1990).
39. B. M. Deb and P. K. Chattaraj, Phys. Rev. A **39**, 1696 (1989).
40. B. M. Deb, P. K. Chattaraj, and S. Mishra, Phys. Rev. A **44**, 1248 (1991).
41. P. K. Chattaraj, Int. J. Quantum Chem. **41**, 845 (1992).
42. B. M. Deb and S. K. Ghosh, J. Chem. Phys. **77**, 342 (1982).
43. L. J. Bartolotti, Phys. Rev. A **24**, 1661 (1981).
44. E. Runge and E. K. U. Gross, Phys. Rev. Lett. **52**, 997 (1984).
45. E. K. U. Gross and W. Kohn, in *Density Functional Theory of Many-Electron Systems*, S. B. Trickey, Ed. (Academic Press, New York, 1991).
46. Bijoy Kr. Dey and B. M. Deb, to be published.
47. B. M. Deb and P. K. Chattaraj, Phys. Rev. A **45**, 1412 (1992).
48. E. Clementi and C. Roetti, At. Data Nucl. Data Tab. **14**, 174 (1974).
49. M. D. Feit and J. A. Fleck, Jr., J. Chem. Phys. **80**, 2578 (1984).
50. C. E. Moore, *Atomic Energy Levels*, (U.S. National Bureau of Standards, Washington, DC, 1949), Vol. 1, pp. 4–8.
51. W. C. Martin, J. Phys. Chem. Ref. Data **2**, 257 (1973).
52. A. K. Das, PhD Thesis (Indian Association for the Cultivation of Science, Calcutta, 1992).
53. D. Ray and P. K. Mukherjee, J. Phys. B: At. Mol. Opt. Phys. **24**, 1241 (1991).